Geochemistry, Geophysics, Geosystems®

AGU ADVANCING EARTH AND SPACE SCIENCE

RESEARCH ARTICLE
10.1029/2021GC009724

Key Points:

- Methane conduits under the seafloor are modeled through the means of a chemical garden laboratory analog
- A hydrate membrane is assumed to exist at the interface between warm methane rich fluid and colder liquid near the surface, affecting flow
- Gulf of Cadiz field samples confirm the existence of centimeter wide conduits as well as authigenic carbonate rocks in methane venting areas

Supporting Information:

Supporting Information may be found in the online version of this article.

Correspondence to:

L. A. M. Rocha and J. H. E. Cartwright, lam99@cam.ac.uk; julyan.cartwright@csic.es

Citation:

Rocha, L. A. M., Gutiérrez-Ariza, C., Pimentel, C., Sánchez-Almazo, I., Sainz-Díaz, C. I., Cardoso, S. S. S., & Cartwright, J. H. E. (2021). Formation and structures of horizontal submarine fluid conduit and venting systems associated with marine seeps. *Geochemistry, Geophysics, Geosystems*, *22*, e2021GC009724. https://doi.org/10.1029/2021GC009724

Received 17 FEB 2021
Accepted 9 OCT 2021

Formation and Structures of Horizontal Submarine Fluid Conduit and Venting Systems Associated With Marine Seeps

Luis A. M. Rocha[1], Carlos Gutiérrez-Ariza[2], Carlos Pimentel[2], Isabel Sánchez-Almazo[3], C. Ignacio Sainz-Díaz[2], Silvana S. S. Cardoso[1], and Julyan H. E. Cartwright[2,4]

[1]Department of Chemical Engineering and Biotechnology, University of Cambridge, Cambridge, UK, [2]Instituto Andaluz de Ciencias de la Tierra, CSIC–Universidad de Granada, Granada, Spain, [3]Centro de Instrumentación Científica, Universidad de Granada, Granada, Spain, [4]Instituto Carlos I de Física Teórica y Computacional, Universidad de Granada, Granada, Spain

Abstract Methane-rich water moves through conduits beneath the seafloor whose surfaces are formed through precipitation reactions. To understand how such submarine fluid conduit and venting systems form and grow, we develop a detailed mathematical model for this reaction-advection system and we quantify the evolution of an ensemble of similar filaments. We show that this growth can be described by a superposition of advection and dispersion. We analyze analog laboratory experiments of chemical-garden type to study the growth of a single filament undergoing a precipitation reaction with the surrounding environment. We apply these findings to geological fluid conduit and venting systems, showing that their irregular trajectories can lead to very effective spreading within the surrounding seabed, thus enhancing contact and exchanges of chemicals between the conduit and external fluids. We discuss how this methane venting leads to the formation of marine authigenic carbonate rocks, and for confirmation, we analyze two field samples from the Gulf of Cadiz for composition and mineralogy of the precipitates. We note the implications of this work for hydrate melting and methane escape from the seabed.

1. Introduction

It is important for climate research to understand how methane escapes from the seabed (Judd, 2003). Under what circumstances might fluid-flow based hydrate melting contribute to climate warming (Cardoso & Cartwright, 2016; Reynolds et al., 2017)? Currently there is no conclusive proof that methane from marine hydrates directly reaches the atmosphere and contributes to global warming, however, further modeling studies and measurements are necessary to provide reliable estimates on the impact of dissociating hydrates on the climate (Kretschmer et al., 2015; Ruppel & Kessler, 2017). Furthermore, methane hydrates represent a vast part of the global methane budget, yet it is still unknown exactly how much of it exists, or what fraction of the hydrates is at risk of dissociation (Buffett & Archer, 2004; Milkov, 2004). Thus it is important to better understand how these hydrates form and spread under the seabed. Any answer to this question must include understanding the advective fluid-flow processes in a marine geological environment where methane hydrates are present (Bohrmann & Torres, 2006; Serov et al., 2017).

The existence of plumbing systems of fluid-filled conduits in the seabed is now widely observed. Methane seeps (Ceramicola et al., 2018) and mud volcanoes are instances in which these processes are active. There is extensive evidence of the existence of methane seeps, in such locations as the Cascadia margin (Baumberger et al., 2018; Collier & Lilley, 2005; Linke et al., 1994; Riedel, Scherwath, et al., 2018; Wood et al., 2002), the Hikurangi margin (Barnes et al., 2010; Riedel, Crutchley, et al., 2018), and the Vestnesa Ridge offshore west Svalbard (Bünz et al., 2012; Hammer et al., 2011; Petersen et al., 2010), among others (Shakhova et al., 2010; Skarke et al., 2014; Solomon et al., 2009). How do these seabed fluid-flow features form (Räss et al., 2018), develop, and eventually terminate? In some cases, we find a central vertical conduit brings fluid, including dissolved and gaseous methane, up from depth in the submarine sediment to the seafloor (Paganoni et al., 2018), where it may disperse into the water column; this can be associated with a submarine mud volcano, a seep, or a seabed pockmark (Cartwright & Santamarina, 2015; Maestrelli et al., 2017). In some cases,

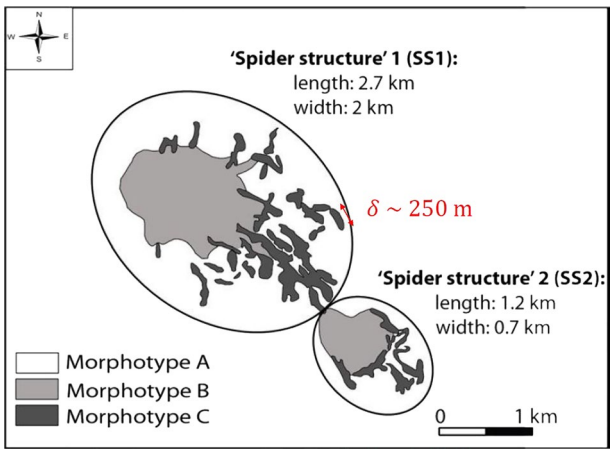

Figure 1. Schematic of geological so-called spider-leg structures found on the Congo continental slope. Morphotype A corresponds to regional background, Morphotypes B and C correspond to the "body" and "legs" of a spider structure, respectively. Original image from Casenave (2017).

however, the exit to the ocean of such a central conduit may become blocked (Ho et al., 2012), owing to what has been termed self-sealing processes (Hovland, 2002). In sea-floor plumbing systems with a blockage of the exit of the central conduit, there may be a layer of methane hydrate blocking the exit and evidence of pressure-induced doming of the seabed (Barry et al., 2012; Koch et al., 2015). Indeed, the overpressure can be such that there have been noted instances of natural hydraulic fracturing—fracking—induced by the geological fluid flow (Blouet et al., 2017). One often finds authigenic carbonate minerals are formed associated with these features; this secondary biomineralization process is of global importance as a carbon sink (Alperin & Hoehler, 2010; Chen et al., 2014; Luff et al., 2004).

Submarine "spider structures" have been observed and described in the literature as pockmark-like seabed venting structures (Casenave et al., 2017); see also Ho et al. (2012) and Maia et al. (2016). These are composed of large quasi-circular depressions, the "body" of the spider, surrounded by more elongated depressions, (the "legs" of the spider, as shown in Figure 1. These "spider legs" measure about 50 m wide and can be several 100 m in length, and are present just below seafloor (Casenave et al., 2017). The entire structure has been found to leak methane into the ocean, with the legs having a greater activity than the body due to the migration of the fluids within the depressions. This pattern suggests that methane is venting to the sea floor and becoming blocked from getting released, so is forced to spread horizontally, concentrating its flow in tubes (Loher et al., 2018). Indeed, a saturated source of methane from depth may form methane hydrates as it cools down upon contact with cooler sediments near the surface. These hydrates will thus form a solid membrane at the interface between the injected warm water with dissolved methane and the cooler host fluids near the surface. As a result, the flow of methane in the cracks of the sediment will be blocked by this membrane; the progress of the injected fluids will involve the successive breaking and formation of methane hydrate along the cracks. This is a possibility already supported by experimental and modeling work (Fu et al., 2020; Meyer et al., 2018, 2020).

While seismic techniques to image sub seafloor stratigraphy show us the existence of large conduit structures, they do not have the resolution necessary to demonstrate the existence of smaller tubes in currently active systems. On the other hand, such smaller tubes are well known from the geological record (Gay et al., 2019; Liang et al., 2016) and are recovered in sampling missions. In the geological literature, we find many observations consistent with such a blocked vertical conduit leading to horizontal spread of fluids. For example, Mazzini et al. (2008) comment, "*The data described indicates that fluids seep vigorously not only vertically but also migrate horizontally*," "*tubular features … branch off … forming a network that extends horizontally in the subsurface*." And Gay and Migeon (2017) describe, "*Most of the pipes are sub-vertical with their length-axis perpendicular or sub-perpendicular to the bedding plane. They are 10 to 40 cm in diameter and 50 cm to 10 m in length. In some cases, they are inter-connected, forming a real plumbing system. A direct comparison with seismic-scale features is still not realistic to manage because their dimensions are far below the seismic resolution … this suggests that a fluid pipe few hundred-meters wide identified on the seismic record is most probably a set of several small-scale pipes together propagating in a large area of sediment impregnated with fluids*." However, neither imaging nor geology can tell us about fluid flow rates. Geologists have performed laboratory experiments in porous media to attempt to understand these observations (Gay et al., 2019; Mazzini et al., 2008), and a numerical model has investigated the clogging of gas hydrate deposits in porous marine sediments (Nimblett & Ruppel, 2003).

Here, we ask how these blocked fluid venting systems develop. We can make much use of a laboratory analog for such a fluid-flow system. Vertical fluid flow in these blocked systems is forced to be planar: when the fluid rising up the central conduit arrives at the blockage it is forced sideways, and so spreads radially. This type of two-dimensional fluid flow is modeled in the laboratory with a Hele-Shaw cell. The spreading of fluid-filled conduits is replicated through the means of precipitation reactions, often referred to as chemical gardens (Barge et al., 2015). Among the flow patterns found in these laboratory flow and precipitation

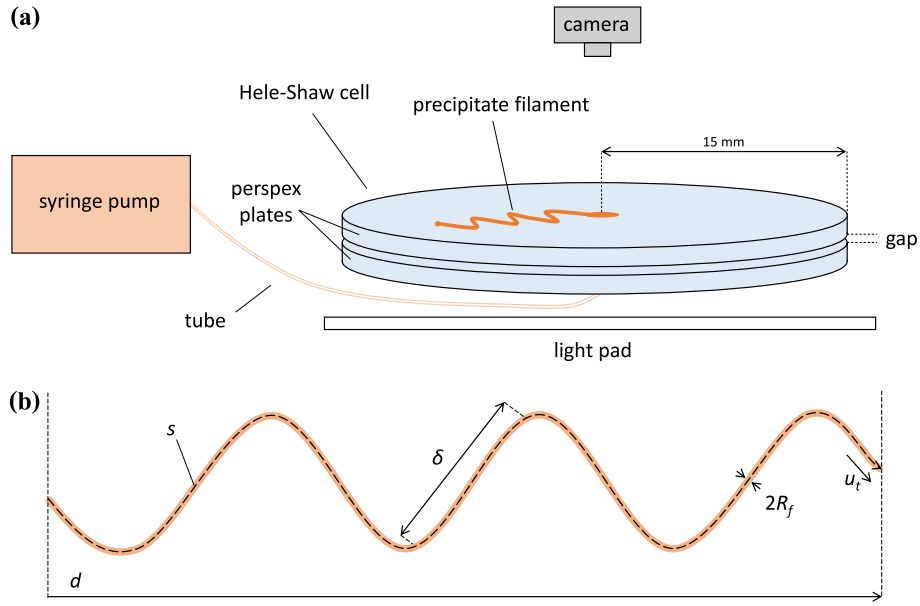

Figure 2. (a) Schematic of the Hele-Shaw cell set-up. A metal salt solution is pumped into a Hele-Shaw cell filled with a host solution of sodium silicate. This leads to the formation of a chemical garden filament with a tip advancing over a tortuous trajectory at a certain speed. Photos of the reaction are taken from above every 2°s. Image analysis allows the determination of the properties of the filament, such as speed, width, and typical distance between turns. (b) Generic shape of a precipitate filament, with the different variables that characterize it: arc length s, Euclidean distance d, typical distance between turns δ, width $2R_f$, and speed of the tip u_t. The active filament tip thus changes direction periodically; a frequency of oscillation can then be estimated from the speed and typical distance between turns, as $f = u_t/\delta$. Figure reproduced from Rocha et al. (2021) with permission from the PCCP Owner Societies.

reactions, filaments (Brau et al., 2018; Rocha et al., 2021) are the most similar to sea-floor conduits, and are studied more closely in this work. We focus on both the growth of a single filament and on the dispersive nature of the motion of an ensemble of similar filaments in a two-dimensional geometry. We show how their structure with erratic turns ensures widespread contact with the surrounding environment, thus facilitating chemical exchanges through their surface. We analyze two field samples of tubular precipitates from the Gulf of Cadiz, their composition and mineralogy. As well as understanding natural seabed fluid-flow features, an accompanying question of great interest at present is whether one might induce the formation of such blockages through geoengineering, in this way arresting the escape of methane from dissociating hydrates into the hydrosphere and instead locking it up in carbonate rock.

2. Laboratory Analog: Planar Chemical Garden Filament Structures

Chemical gardens are precipitation structures that form when a metal salt comes into contact with an aqueous solution containing anions such as silicate, carbonate or sulphate, among others (Barge et al., 2015). Several methods of growth of these structures exist, with the common characteristic among them being the formation of a semipermeable precipitation membrane at the interface of the two reactants, across which steep concentration gradients are established. These then lead to osmotic and buoyancy forces which affect the development of the structure. Chemical gardens are thus formed out of a self-organizing non equilibrium process, and are found in a variety of settings, such as filiform corrosion, cement hydration and hydrothermal vents (Barge et al., 2015). These structures can be grown in Hele-Shaw cells, which consist of a reactor made up of two parallel plates separated by a small gap, creating a quasi-two-dimensional space, as shown in Figure 2. By varying the concentration of the reactants and the flow rates of injection into the cell, a wealth of different patterns can be observed. One of the most prominent patterns are filaments, thin tubes that grow with an erratic, zig-zag trajectory. The motion of the tip of these filaments has been successfully modeled by considering the diffusive supply of metal salt ions to the outer surface of the membrane, where they react to form more product; and the spreading of precipitate along the perimeter of the membrane. A

detailed experimental and modeling analysis of these filaments was the basis of a previous published study (Rocha et al., 2021).

An understanding of the processes taking place in metal-salt chemical gardens has given the new field of chemobrionics (Barge et al., 2015; Cardoso et al., 2020). In chemobrionic systems, the components can be a wide variety of reactants. In this work, this chemical garden system is shown to be analogous to the submarine venting systems, and the mathematical model developed for the precipitate filaments, described in the following section, is then applied to the specific case of the spider structures.

3. Mathematical Modeling

The model (Rocha et al., 2021) considers the dynamics at the tip of a moving filament, by establishing a balance between the concentration of solids produced by precipitation, c, and the pressure difference p across the membrane.

Ions diffuse with coefficient D_m across a length scale L_r to the outer surface of the membrane, where they react to produce more solid. As ions are consumed by reaction, a concentration gradient is established over that length scale. At the same time, spreading due to outflow leads to a dilution of the concentration of these solids across the perimeter of the membrane, with curvature K. The Heaviside step function is present since product is only formed when there is outflow of metal salt ions. The variation in p is dependent on the change of volume of fluid at the tip of the filament and the deformation of the membrane γ. This parameter is a function of the physical properties of the membrane material, the Young's modulus and Poisson ratio (Rocha et al., 2021; Turcotte & Schubert, 2002). This is expressed mathematically as follows:

$$\frac{dc}{dt} = \left(\frac{D_m}{{L_r}^2} c_{ms} - \kappa u_t c\right) \mathcal{H}[u_t], \tag{1a}$$

$$\frac{dp}{dt} = \gamma Q_i - u_t \left(\gamma A_{out} + \alpha Q_i\right) \tag{1b}$$

where c_{ms} is the concentration of the metal salt ion. Q_i is the flow rate of metal salt solution flowing inside the filament, A_{out} is the cross sectional area of the filament, and α is the pressure drop across its length. The speed of the filament is u_t; since a pressure difference p is established across a porous membrane of thickness L_m, advection over this medium is given by Darcy's law:

$$u_t = \frac{k_{out}}{\mu} \frac{p}{L_m} \left(1 - \frac{c}{c^*}\right) \mathcal{H}\left[1 - \frac{c}{c^*}\right]. \tag{2}$$

where μ is the dynamic viscosity of the fluids without product, k_{out} is the permeability of the membrane (Cardoso & Cartwright, 2014; Kedem & Katchalsky, 1958; Turcotte & Schubert, 2002) and L_m its thickness. The parameter c^* indicates the dependence of outflow on the concentration of solids at the interface of the two fluids: as c grows, u_t decreases and ceases when it reaches the critical product concentration c^* (Wagatsuma et al., 2017).

Substituting the speed relations (2) into the governing Equation 1 and non-dimensionalizing using the scales for time $t_s = \mu L_m/(\gamma A_{out} k_{out})$, pressure $p_s = \gamma A_{out}/\kappa$ and concentration $c_s = c^*$, leads to the following simplified coupled equations,

$$\frac{d\hat{c}}{d\hat{t}} = (M - (1 - \hat{c})\hat{p}\hat{c})\mathcal{H}[1 - \hat{c}], \tag{3a}$$

$$\frac{d\hat{p}}{d\hat{t}} = N - (1 + W)(1 - \hat{c})\hat{p}\mathcal{H}[1 - \hat{c}]. \tag{3b}$$

The evolution of the system depends on three non-dimensional groups:

$$M = D_m \mu L_m c_{ms}/(k_{out} A_{out} \gamma {L_r}^2 c^*)$$

is a non-dimensional rate of accumulation of solid;

$$N = \mu L_m \kappa Q_i/(k_{out} \gamma {A_{out}}^2)$$

is a non-dimensional volumetric injection rate of metal ion;

$$W = \alpha Q_i/(A_{out}\gamma)$$

measures the pressure drop along the filament.

Linear stability analysis of the governing equations shows that the system can be stable, unstable, and oscillatory. The filament regime observed experimentally has been identified as corresponding to the oscillatory behavior of the model, as the constant variation of c and p leads to the erratic trajectories of the filaments. The frequency of oscillation f can be derived as

$$f = \frac{(-F/4)^{1/2}}{2\pi t_s} \tag{4}$$

where

$$F = 4M - 4N + 4MW + \left(\frac{MN}{M - N + MW} - \left(\frac{M(W+1)}{N} - 1 \right)(W+1) + \frac{N^2 \left(\frac{M(W+1)}{N} - 1 \right)}{(W+1)(M - N + MW)} \right)^2 . \tag{5}$$

The three dimensionless numbers will determine the behavior of the system: in the unstable regime no filaments are formed and the precipitate spreads radially, in the oscillatory regime a filament advances with periodic changes in its direction (the stable regime predicts a filament that moves straight, however, the conditions for the formation of such a filament are not available with this experimental setup [Rocha et al., 2021]). The frequency of oscillation f can also be determined experimentally, as demonstrated in Figure 2, allowing the comparison of theory with data.

The behavior of these chemical garden structures can also be analyzed in terms of the statistical mechanics of an ensemble of filaments. Indeed, the random motion of each active filament tip leads to a variation in the distance between a given filament tip and the position of an ensemble of tips. This can be shown to produce a dispersion in the motion of an ensemble of filaments that scales as follows:

$$D_e \sim c_D u_t \delta \tag{6}$$

where c_D is a constant. The dynamics of a chemical garden filament system can thus be assigned a dispersion coefficient D_e, analogous, for instance, to the dispersion of a solute in a porous medium (Phillips, 1991).

We now consider the same mechanism occurring in submarine methane venting conduits: instead of a metal salt filament advancing in a silicate solution and separated by a precipitate membrane, we analyze a hydrate membrane at the interface between an advancing stream of warm methane saturated fluid and colder water near the surface. The assumptions behind this application and the estimate of the relevant parameters are explained in the following section.

4. Application to Methane Venting Spider Structures

4.1. Assumptions of the Model

In the chemical garden experiments, the time scale for the formation of precipitate is considered negligible. It is important to analyze if the same assumption can be made in the spider structures. The process of methane hydrate formation first involves nucleation, where stable hydrate nuclei are formed from a supersaturated solution, and then growth, where these nuclei grow and agglomerate. The period between the establishment of supersaturation and the formation of the first nucleus of critical size, which may spontaneously grow to a macroscopic size, is referred to as the induction time.

For heterogeneous nucleation, the following empirical equation has been proposed based on measurements made in a stirred reactor (Natarajan et al., 1994):

$$t_i = K^* \left(\frac{f}{f_{eq}} - 1 \right)^{-m^*} \tag{7}$$

where for methane, $K = 311.64$ s and $m = 1.21$ (Natarajan et al., 1994). Methane hydrates are found in the spider legs (Casenave et al., 2017) at a depth of 600–700 m on the Congo continental slope, so that considering the geotherm (Sultan et al., 2004), the temperature is approximately 280 K and the hydrostatic

Table 1
Properties of the Spider Legs

Properties of the carbonate rocks in which the methane hydrates flow		
D_m	Mass diffusivity	10^{-9}m^2 s^{-1}
E	Young's modulus	10^9 Pa
ν	Poisson ratio	0.5
σ	Porosity	0.2
μ	Viscosity (water)	10^{-3} Pa.s
Properties of the precipitate membrane		
L_m	Thickness	4.8×10^{-5} m
k_{out}	Permeability	2.0×10^{-12} m^2
Lr	Length scale of reaction	7.2×10^{-5} m
Size of the cracks		
R_f	Radius of a crack	1.0×10^{-2} m
H	Width of a crack	2.0×10^{-2} m
A_{pore}	Cross section area of a crack	3.1×10^{-4} m^2
Dimensions of the spider legs		
R_s	Radius of spider leg	25 m
H_s	Width of spider leg	50 m
A_s	Cross section area of spider leg	2.0×10^3 m^2
δ	Typical distance between turns in a spider leg	250 m
Flow rate in a spider leg		
q_s	Flux in a spider leg	1,000 m year^{-1}
		3×10^{-5} m s^{-1}
Q_s	Flow rate in a spider leg	6.2×10^{-2} m^3 s^{-1}
n_c	Number of cracks	1.3×10^6
Q_c	Flow rate in a crack	5.0×10^{-8} m^3 s^{-1}
Concentration of dissolved methane and critical product concentration		
C	Methane concentration	110 mol m^{-3}
C^*	Critical product concentration	3,000 mol m^{-3}
Values obtained from the properties presented above		
v	Fluid velocity in a spider leg	3.2×10^{-5} m s^{-1}
α	Pressure drop along spider leg	2.6×10^5 kg m^{-5} s^{-1}
K	Curvature of membrane in a pore	100 m^{-1}
γ	Deformation of membrane	1.1×10^6 kg m^{-5} s^{-1}

pressure is 7.1 MPa (Casenave et al., 2017). For these conditions, using the Peng–Robinson equation of state (Peng & Robinson, 1976) to calculate the fugacities, Equation 7 yields an induction time of approximately 1,100 s. Such a time is negligible compared with the time of lifetime of a spider leg, which we estimate from the advection time in the spider legs as $L_{spider}/v = 1.6 \times 10^7$s (185 days) for a leg with a typical length of 500 m and fluid velocity of 3.2×10^{-5} m s^{-1} (see Table 1). However, after the first nucleation, the induction time is expected to reduce drastically owing to the presence of small secondary hydrate nuclei (Giavarini et al., 2003; Lee et al., 2005; Linga et al., 2007; Monfort & Nzihou, 1993; Parent & Bishnoi, 1996; Ribeiro & Lage, 2008; Sloan & Koh, 2007; Vysniauskas & Bishnoi, 1983). This memory effect has been used to explain

the seemingly very fast nucleation of hydrates coating methane bubbles released from the seafloor (Rehder et al., 2002). A higher rate constant is relevant to explain the very fast formation of hydrates around methane bubbles at the bottom of the ocean; bubbles are reported to become fully covered in hydrate in times of at most 23 s (Gumerov & Chahine, 1998; Lee et al., 2005; Rehder et al., 2002). We expect that this is also the case for the spider structures, suggesting that after a rapid nucleation, it is growth of the hydrate that determines the dynamics at the tip of the spider legs.

Numerous experimental studies in semi-batch reactors have focused on the hydrate growth rate at the interface between liquid saturated with methane and the gas phase. Early results by Englezos et al. (1987) predicted the intrinsic kinetic rate for a range of temperatures and pressures. Later work (Skovborg & Rasmussen, 1994), however, suggested that the growth of hydrate is limited by the transport of methane in the liquid film at the interface with the gas. Thus, gas is transported with diffusivity D_m across the film with thickness L_r. It was shown that a mass transfer coefficient of 5×10^{-5} m s^{-1} reflects the experimental measurements accurately. Herri et al. (1999) presented another model for hydrate growth in agreement with these findings.

Methane hydrate grows at the tip of a spider leg by cooling of the saturated solution as it contacts the colder outside environment together with diffusion of methane from the interior of the leg to the tip. We estimate the mass transfer coefficient for the transport of methane to be $k_L = D_m/L_r \sim 1.4 \times 10^{-5}$ m s^{-1}. Along with other properties of these submarine venting structures, L_r was estimated in Section 4; all properties are summarized in Table 1. Since this coefficient is smaller than in the experiments of Englezos et al. (1987), which were shown to be mass-transfer limited, we conclude that the growth of hydrate is limited by diffusion of methane across the film where reaction takes place. The diffusive or growth timescale is then $t_g = {L_r}^2/D_m \sim 5$ s.

We thus establish that the formation of methane hydrate at the tip of a spider leg is limited by the diffusion of methane within the leg to its tip, and this is analogous to the growth of precipitate filaments in chemical gardens.

One of the assumptions of the model is that the hydrates form a precipitate membrane at the tip of the leg, at the interface between different fluids. Given that the leg is narrow, compared to length, one could expect it to cool from the sides to the center relatively fast, over a timescale similar to the estimate for the timescale for advection of methane along a leg. This would suggest that the entire structure should become saturated with hydrates, thus blocking the flow. However, the spider structures are explicitly described to grow over time, with the elongated legs being more recent than the sub circular body of the structure. Furthermore, the more active methane venting sites are found on the newer sections of the structure, near the extremities of the spider legs. Observations clearly suggest that methane flows from the center of the structure to the tips of the legs, where it then migrates to the seafloor where it is released. Thus, blocking of flow only ever occurs at the tip of the spider legs.

In addition, the model assumes that the liquid phase is saturated with methane, with no gas phase present. This is supported by the fact that no bubbles were found escaping from the seafloor in the area of the spider structures; these leak dissolved methane into the water column (Casenave et al., 2017). In spite of this, methane bubble releases from seeps are often observed; varying amounts of bubbles can emerge from the seafloor and into the water column, with diameters typically in the range of 3–5 mm (Di et al., 2019; Todd & MacDonald, 2017). The size and number of bubbles present in the conduits may influence the dynamics of the system. If small bubbles form and move to the top of the conduit and get trapped there, and slowly get released upward, then it is just saturated liquid that moves horizontally. If the bubbles coalesce and form a slug, it moves at a slower speed than the liquid and preferentially at the top of the conduit (Brennen, 2005; Talimi et al., 2012). Under these cases, the model described here may still be valid, with the gas phase merely reducing the effective cross sectional area of the tubes. On the other hand, if very large numbers of bubbles are present, these may form a liquid foam (Weaire & Hutzler, 2001) or block the pores and fractures, forcing the liquid to change trajectory. Investigating the nature of the gas phase in methane conduits may be a relevant avenue for future work, which may allow for more accurate models.

Recently published models for the migration of methane gas across the hydrate stability zone have introduced the concept of crustal fingering (Fu et al., 2020; Meyer et al., 2020), which has several points

in common with the model proposed here. Both consider the formation of a rigid thin hydrate crust at an interface, which serves as barrier to flow. Under the crustal fingering model, methane spreads in fingers as the hydrate crust is ruptured, allowing for gas to flow, which then forms more hydrate at the gas-liquid interface. The rupturing is caused by the pressure difference that is established across the hydrate crust. The mechanism then repeats periodically, with the gas moving in a filament/finger shape until it stops due to reduced driving pressure and thickening of the crust. The main difference in the model used in this work is that it does not actually consider any ruptures of hydrates crusts, but rather a variation in the concentration of hydrate in a membrane at the interface, which affects the resistance to the passage of methane gas. Additionally, crustal methane fingers are reported to measure about a millimeter wide or less, while here we assume flow in fractures in the sediment a few centimeters in width.

5. Estimate of the Model Parameters

While initially derived for the chemical garden experiment depicted in Figure 2 (Rocha et al., 2021), these equations can be adapted to the submarine spider structures. In order to apply the model to the spider legs, it is necessary to estimate some of the physical and chemical properties, presented in Table 1. The values of mechanical properties of methane-hydrate-bearing sediments (Zhang et al., 2012) and the porosity and permeability of carbonate rocks (Rashid et al., 2015; Shah et al., 2013) may be obtained from the literature. The Young's modulus of methane hydrate has been reported to be of the order of 10^9 Pa (Gabitto & Tsouris, 2010; Shimizu et al., 2002). The methane flow rates within the spider structures may be estimated considering the typical scales of methane fluxes in marine seeps (Cardoso & Cartwright, 2016; Reeburgh, 2007). The concentration of methane, c, in the saturated warm water feeding the spider structures was taken to be 110 mol m^{-3} using correlations for the solubility of methane in water (Lu et al., 2008; Tishchenko et al., 2005). Assuming the hydrates are present at a depth of 775 m (Casenave et al., 2017), the water is expected to be at 283 K and a pressure of 7.8 MPa, with the typical seawater salinity of 35 parts per thousand. This value of c is in agreement with estimates of methane concentrations in sediments under methane hydrates (Davie & Buffett, 2003; Davie et al., 2004). The variable c^* represents the concentration of product that blocks the flow in the model. No obvious equivalent of this variable is available for the spider leg. The permeability of porous media with methane hydrate has been reported to drop steadily with increasing methane hydrate content, until a value of 40% hydrate saturation of pore space, above which permeability seems to stabilize (Liang et al., 2011). Assuming 40% of methane hydrate saturation to correspond to c^*, and taking into account the molar volume of methane hydrate (Anderson, 2004), we estimate $c^* \sim 3000$ mol m^{-3}. While this is an estimate, the actual value of c^* is certainly within the same order of magnitude and different ratios of hydrate saturation do not significantly alter the results, that is, the values of M and $f.ts$ remain in the same order of magnitude and with comparable values to those of the chemical garden filaments.

Observed cracks in the sediment have been reported to be in the size range of 5–20 mm (McMahon et al., 2016). We shall consider flow in a crack with centimeter scale radius in the predictions below (see Table 1). Assuming that these cracks have a circular cross section, the parameter γ will include the deformation ω of a thin circular plate with supported edges under uniform pressure (Timoshenko & Woinowsky-Krieger, 1959),

$$\omega = \frac{p(R^2 - r^2)}{64D}\left(\frac{5+\nu}{1+\nu}R^2 - r^2\right), \tag{8}$$

where p is the pressure, R is the radius of the plate, r is the radial distance from the center of the plate, D_{fr} is the flexural rigidity and ν is Poisson's ratio. All these values are summarized in Table 1.

This set of properties for the spider legs leads to values of M, N, and W of 0.51, 1.13, and 3.79×10^{-5} respectively, as well as a value of ts of 71.3 s. The dimensionless numbers are of the same order as the ones for the laboratory experiments, as illustrated in Figure 3a. This means that if the model can indeed be applied to submarine conduits as described in this work, these structures should be expected to behave in a similar manner to the filaments observed experimentally; it is then possible that oscillations in pressure and position occur at the tip of a spider leg as it advances. The frequency of oscillation of the chemical garden filaments is also compared in non-dimensional form with the hypothetical value of f for the spider legs, as shown in Figure 3b. This property is also similar in both cases.

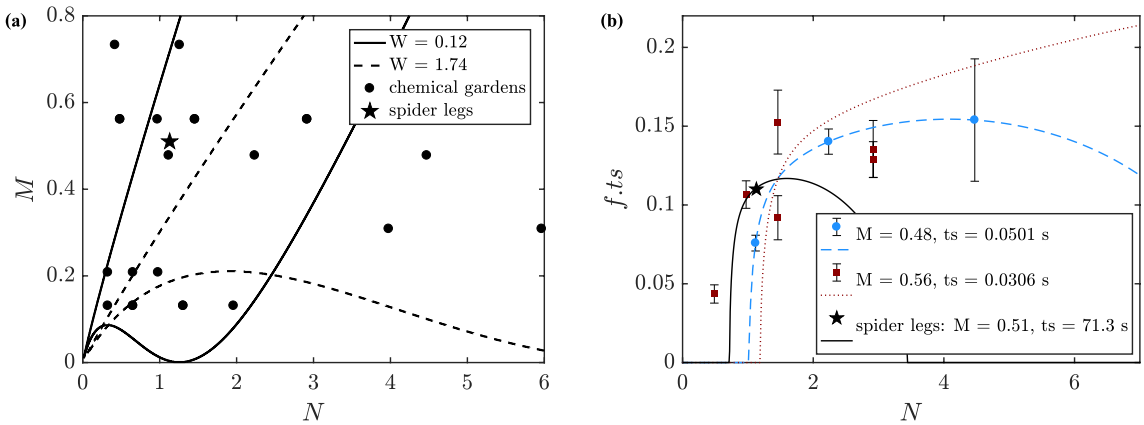

Figure 3. Non-dimensional comparison of the model predictions for the laboratory precipitate filaments and the geological spider structures. (a) Comparison of the values of the dimensionless groups M and N. The lines represent the boundaries of the oscillatory regime. The lines presented correspond to the lowest (solid) and highest (dashed) W in the experimental range. (b) Comparison of the non-dimensionalized frequency of oscillation as a function of N for the spider legs and precipitate filaments grown experimentally with similar values of M. The lines correspond to the model predictions. Both plots show an overlap between the experimental data and the prediction for the spider legs, suggesting that these two systems may behave in a similar manner if the model assumptions are valid.

It is possible to estimate the value of the dispersion coefficient of the spider legs, as described in Section 3 and the literature (Rocha et al., 2021). From the published images of the structures (Casenave et al., 2017), such as the one in Figure 1, spider legs appear to have a typical distance between turns of around 250 m. Considering the average value of c and the estimated fluid velocity of 3.2×10^{-5} m s^{-1}, we come to a value for the dispersion coefficient of 6.3×10^{-4} m^2 s^{-1}. This point is shown together with the experimental values in Figure 4.

We should also comment on the grouping of cracks to form a spider leg. Why do all these flows synchronize left/right? Key here is the coalescence of jets/plumes that are sufficiently closely spaced. Plume coalescence in porous media is discussed in the literature (Cooper et al., 2014; Le Borgne et al., 2013; Ye et al., 2015). For breaks in the membrane that are close enough the ejected fluid coalesces into a single jet. The opposite case is then a mechanism for the bifurcation of filaments. In the lab experiments, bifurcation is rare, but it is observed (Brau et al., 2018; Rocha et al., 2021). In the geological setting, with great dimensions, bifurcations can be more common. Eventually one should get a bifurcating series of filaments that end at small branches, like a tree.

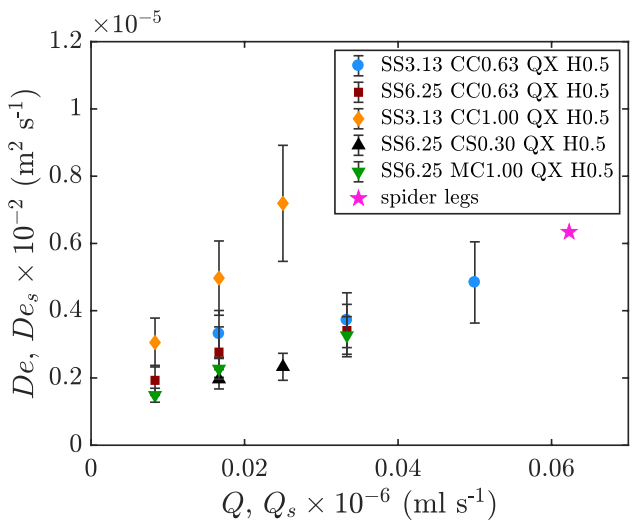

Figure 4. Dispersion coefficient as a function of flow rate for laboratory precipitate filaments (De) and geological spider legs (De_s). Given the different magnitude of the values for the precipitate filaments and the spider legs, the axes have a different scale for these two variables. While the model parameters are very similar in the two cases, the values of the dispersion coefficient are quite different, due to the much larger scale of the spider structures compared to the laboratory filaments.

In Section 7 we investigate samples from the Gulf of Cadiz. They are of tubes with internal diameter of a few centimeters; much less than the tens of meters of the main tubes imaged in geophysical surveys (Casenave et al., 2017). In understanding how one gets from the very large tubes to these smaller tubes, this bifurcation mechanism is the missing part of the argument.

6. Formation of Biomineral Carbonates

An important geological issue to take into account is how the flow in the spider legs may affect the activity of microorganisms that decompose methane. This process is referred to as anaerobic oxidation of methane (AOM), in which a microbial consortium consumes methane and reduces sulphate, producing hydrogen sulphide and bicarbonate, and stimulates the precipitation of carbonate biominerals (Alperin & Hoehler, 2010; Chen et al., 2014). This occurs at the sulphate-methane transition zone (SMTZ), where methane delivered from below by methanogens meets sulphate diffusing from sea water (this is the case for biogenic methane,

it may also be of thermogenic origin, but most commonly at depths greater than 1,000 m (Floodgate & Judd, 1992)). Areas of high methane decomposition may thus be identified by the presence of quantities of methane derived authigenic carbonate rocks on the seabed and past positions of buried SMTZs (Casenave et al., 2017; Luff et al., 2004). These carbonates can also be found at past positions of buried SMTZs. The depth of the SMTZ may change as sulphate is consumed, and may reach the surface if all of it is consumed, leading to the release of methane into the ocean (Casenave et al., 2017). In addition, if large quantities of methane are being supplied from dissociating methane hydrates, hydrate cannot form fast enough and methane may bypass the AOM zone and escape into the water (Treude et al., 2003). More frequently, seeps are not fed by dissociating hydrate but rather by deep advecting fluids originating from fractures caused by tectonic activity, natural reservoir overpressure, or variable inputs of organic carbon (Foschi et al., 2020; Joseph, 2016; Reeburgh, 2007). The rates of AOM have been extensively studied, both through direct in situ measurements and via numerical modeling of concentration data, These range from 10^{-9} M s^{-1} to 10^{-15} M s^{-1}, and are intrinsic to the depth into the sediment and the type of microorganisms present (Barker & Iversen, 1985; Reeburgh, 1980; Treude et al., 2003, 2007; Ussler & Paull, 2008). Methane concentration is often highest just below the AOM zone, and can go up to 10 mM (Barker & Iversen, 1985; Reeburgh, 1980; Treude et al., 2007; Ussler & Paull, 2008). AOM is reported to also occur in the spider structures. Visual observation and sampling reveals carbonates resulting from AOM at or just below the seabed (Casenave et al., 2017). These carbonates stand just above the microbial consortium supplied with methane by the fluid conduits coming from below.

In this work, the chemical garden experiments are used as an analogy for the dynamics of methane hydrate spreading specifically, and as such are not directly linked to the formation of carbonates. However, one relevant characteristic of chemical garden precipitates is the layering of different patterns across their walls and membranes, which may hypothetically be investigated as a parallel to the zonation of carbonates. Indeed, the thickness of chemical garden membranes is a time dependent variable, growing thicker with time. Across this membrane distinct colors can be seen, owing to different oxidation states of the metal ions used in the reaction (Ding et al., 2019). Furthermore, the various patterns that can be observed experimentally are strongly dependent on the local flow velocity; variations in this velocity thus lead to different patterns emerging successively (Ziemecka et al., 2020). Similarly, authigenic mineral formation by AOM involves the precipitation of different carbonates over a series of stages of reaction (Xu et al., 2017; Wei et al., 2021). The manner in which microbial action can transform a chemical-garden precipitate, and how the microorganisms influence the chemical and microstructural characteristics of that precipitate, is being investigated in a different oceanic context, that of rusticles formed on sunken iron-hulled ships (Silva-Bedoya et al., 2021), and findings regarding the role of bacteria in the alteration of the precipitate learned there might be applied to this application in future.

7. Structure of Field Samples

Methane-derived authigenic carbonates have been noted from many regions of the oceans (Feng & Chen, 2015; Prouty et al., 2016), in tubular morphologies as well as other morphologies such as mounds (O'Reilly et al., 2014). Tubular methane-derived authigenic carbonates from the Gulf of Cadiz of 1–35 cm diameter have been characterized (Magalhães et al., 2012); here, we analyze two samples from this region; Figure 5. The tube samples were collected during the 2000–2001 Anastasya cruises in the Gulf of Cádiz (Díaz-del Río et al., 2001). A full description of the sizes and shapes of the tubes can be found in Díaz-del Río et al. (2003). This study on the carbonate chimneys recovered from the area describes "*Large chimneys falling southwards and radially from a sub-circular structure, probably the feeder channel. This suggests the formation of several chimneys from the same conduit.*" as well as "*Carbonate slabs underlie superficial sandy sediments with ripple marks.*" (Díaz-del Río et al., 2003). These findings suggest that carbonate slabs may be blocking vertical flows, and that samples recovered from the area may be from quasi-horizontal tubes emerging from a vertical feeder conduit. It is thus quite plausible that the samples analyzed here correspond to horizontal tubes.

The tubes analyzed have walls of 2–3 cm thickness, an external diameter of 20 cm and a height of 50–100 cm. They have a cylindrical form in general with a compact internal structure. Tubular carbonates of diameters of several centimeters to meters are likely subsurface plumbing systems, but we do not have data

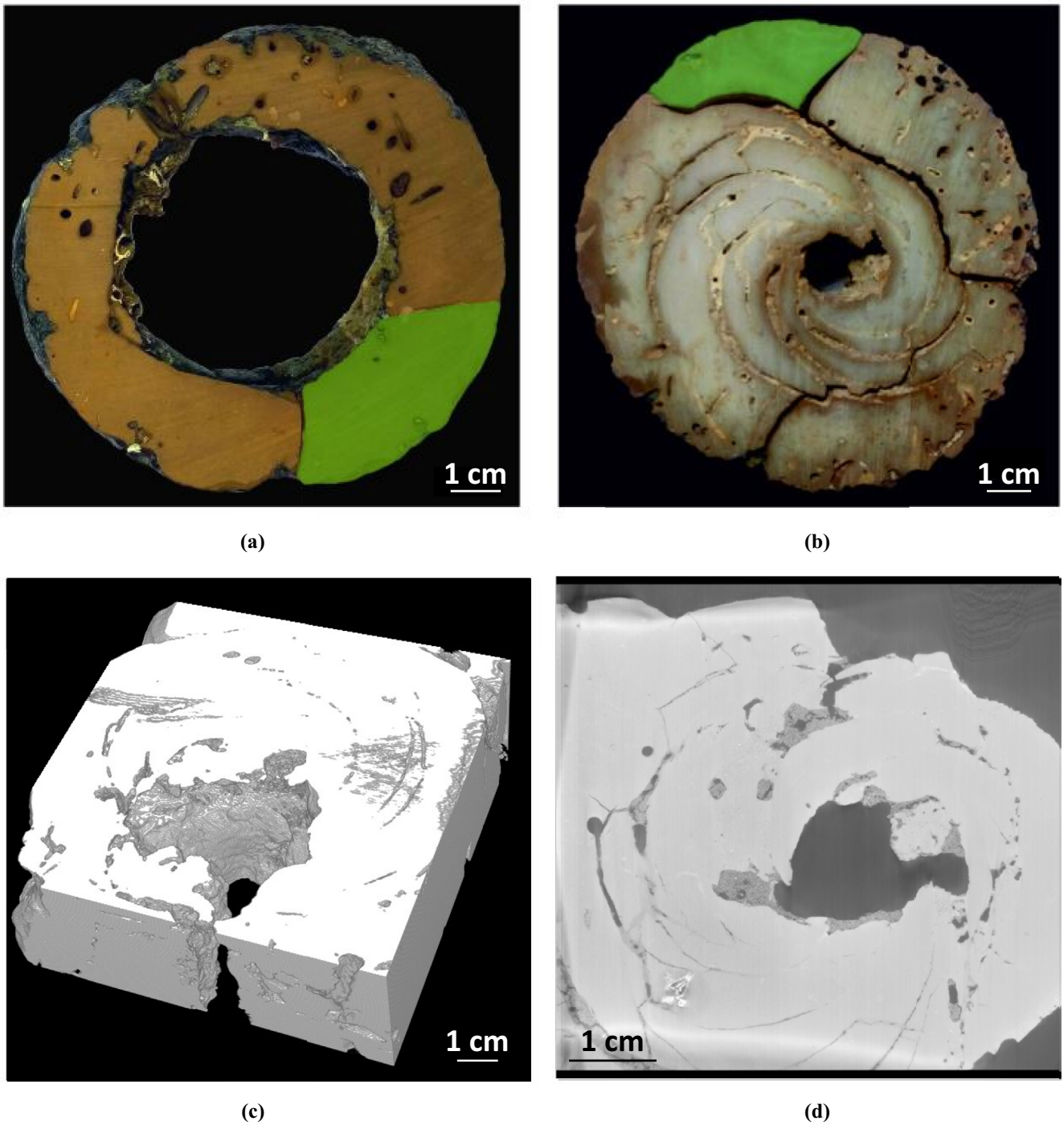

Figure 5. Field samples from the Gulf of Cadiz. (a) Sample with cylindrical morphology; marked in green is the region used for compositional analysis. (b) Sample with helicoidal morphology; again, the region used for compositional analysis is marked in green. (c, and d) 3D X-ray tomography of the helicoidal field sample; see the Supporting Information S1 for the complete tomography.

on their orientation in situ. (It should also be noted that tubes of small diameter, less than a centimeter, may also be biogenic, produced by the burrowing activities of marine organisms [Sun et al., 2020].) The external surfaces of the external and internal parts of tubes have a rough texture. The internal section has low porosity and a color gradient is observed. Helicoidal growth can be appreciated internally in one of the two tubes (Figure 5 and additional figures in Supporting Information S1). An interface is detected between

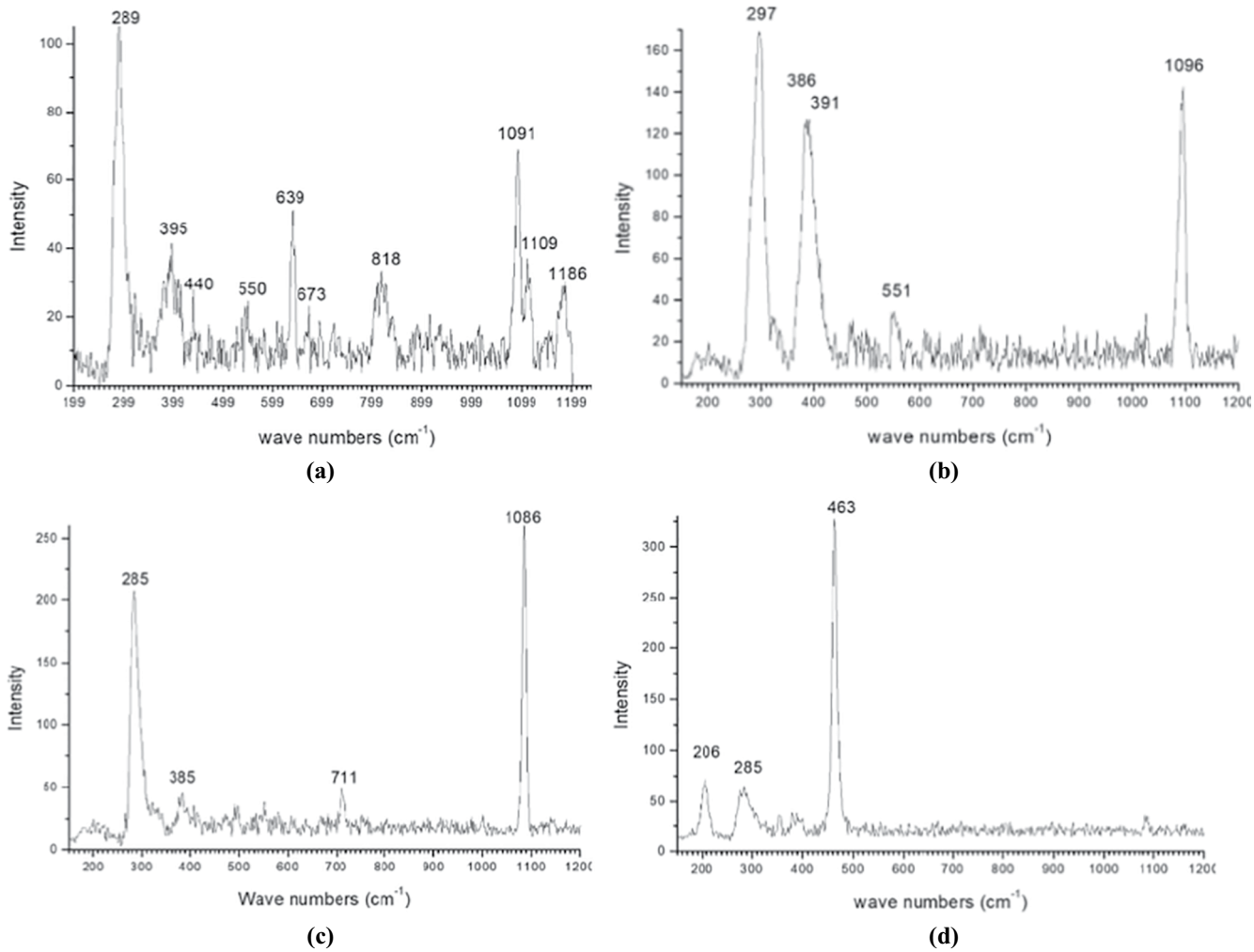

Figure 6. Raman spectra of the field samples. Panel (a) from a polished thin layer of a section of the cylindrical tube; (b, c) different points of the ochre colored zone of a section of the helicoidal tube; and (d) gray color particle localized in the latter zone (optical microscope images can be found in Supporting Information S1).

the bands that form the helicoidal pattern. This interface is filled with sedimentary material. Details of the experimental analysis techniques are described in Supporting Information S1.

A deeper analysis demonstrates the composition as being predominantly of carbonates. Raman spectroscopy (Figure 6) shows a band at 1,091 cm^{-1} and another at 289 cm^{-1} that could indicate the presence of Magnesian calcite (Borromeo et al., 2017; Herman et al., 1987). The shoulder at higher frequencies of the band at 289 cm^{-1} may correspond to iron oxi/hydroxide, goethite (298 cm^{-1}) and the bands at 395, 440, and 550 cm^{-1} indicate also the presence of goethite. The band at 639 cm^{-1} can be assigned to manganese oxides, and the band at 1,109 cm^{-1} can be assigned to dolomite (Figure 6a). In some zones, there can be detected crystals of dolomite (Figure 6b) with bands at 297, and 1,096 cm^{-1} and magnesian calcite (Figure 6c) with bands at 285, 711, and 1,086 cm^{-1}. Some particles of quartz can be detected with bands at 206 and 463 cm^{-1}, along with magnesian calcite, whose bands are at 285 and 1,085 cm^{-1} (Figure 6d). Hence, some differences in the mineral composition can be observed between the cylindrical and helicoidal tube samples.

X-ray diffraction (XRD) analysis of the section of these tubes shows the presence of dolomite (Figure 7). The reflections of calcite have a slight shift to a magnesian calcite, confirmed above by Raman spectra. Probably there is mainly magnesian calcite with small zones of calcite due to the presence of included fossils (see below). In the external surface of the tube, the presence of pyrite and cuprite are also detected, masked with the goethite reflections (Figure 7a). In the gray zones of the section of the helicoidal tube the amount of

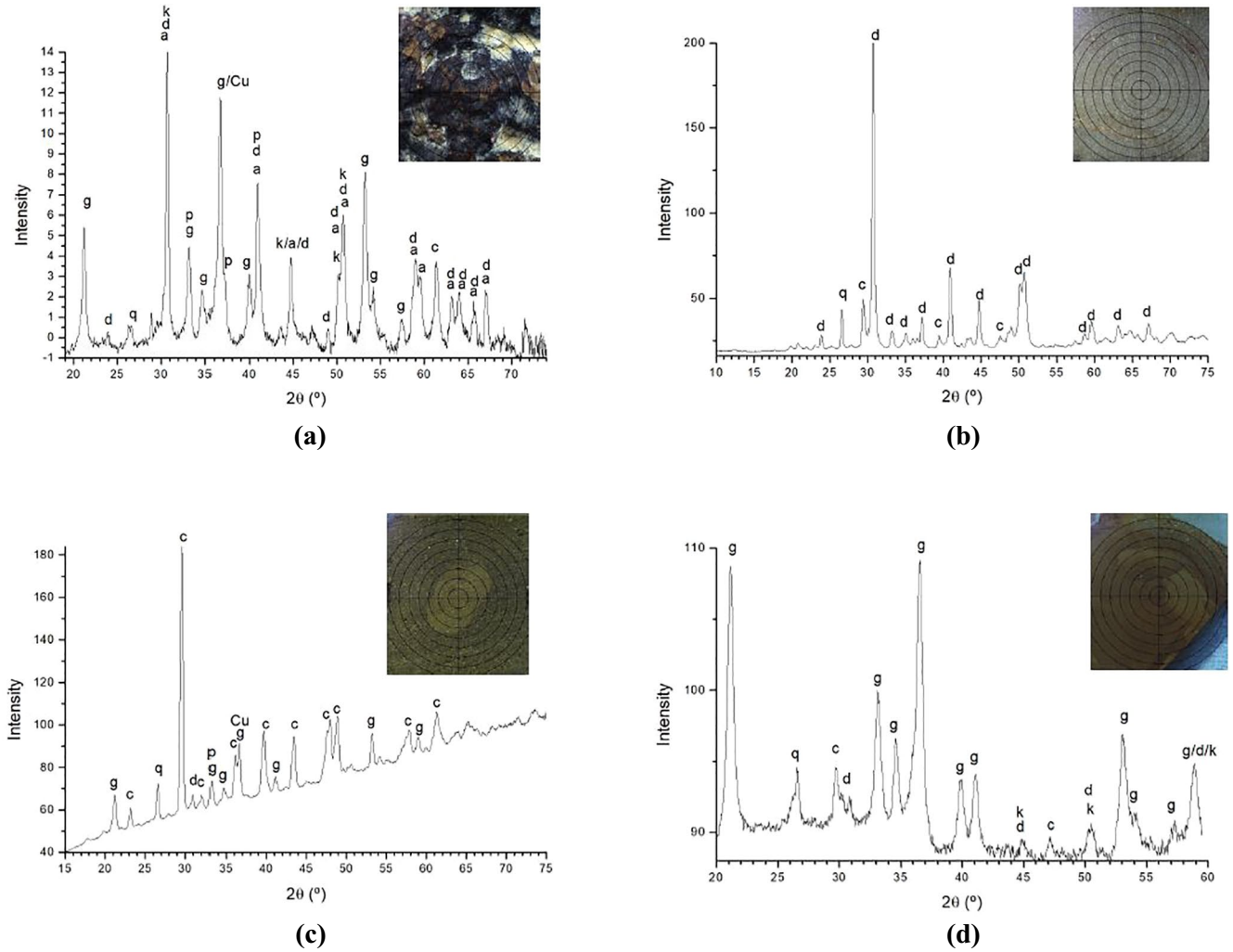

Figure 7. X-ray diffractograms of several sections of the field samples. Images of the analysis points of the samples are included. The labels a, c, d, g, k, p, q, Cu indicate reflections of ankerite (PDF card: 83–1,531), calcite (PDF card: 72–1,651)/magnesian-calcite (PDF card: 86–2335; 86–2336), dolomite (PDF card: 74–1,687), goethite (PDF card: 29–713), kutnohorite (PDF card: 43–695; 84–1,220), pyrite (PDF card: 42–1,340), quartz (PDF card: 79–1,910), and cuprite (PDF card: 77–199). (a) External surface of the helicoidal tube; (b) gray zone of the internal section of the helicoidal tube; (c) ochre colored zone of the internal section of helicoidal tube; and (d) internal section of the cylindrical tube.

iron oxide is lower, there being observed mainly reflections of dolomite and calcite (Figure 7b). The (101) reflection of quartz is detected coming from sandy sediments. In the ochre colored zones of the section of the helicoidal tube, the content of goethite is higher, along with calcite or magnesian calcite (Figure 7c). In the brown section of the cylindrical tube, the main crystallographic phase is goethite, along with quartz and kutnohorite-dolomite, and calcite (Figure 7d). In these diffractograms, we cannot distinguish the reflections of double carbonates, like kutnohorite, and dolomite; see below. These results confirm those discussed above in the Raman spectra. No great compositional differences were observed between the cylindrical and helicoidal tubes, though the cylindrical one has more content of goethite.

ESEM micrographs of a section of the cylindrical tube (Figure 8) show many bands with different brightness. The brightest zones are richer in iron. There are clear domains very rich in iron without calcium and other domains clearly distinguishable that are rich in calcium. Nevertheless, the zones rich in calcium have a certain amount of iron and, surprisingly, manganese. These maps and the above analyses confirm the iron-rich zones are goethite. Some grains rich in manganese have no detectable iron. These grains can be kutnohorite (manganese carbonate) detected above by XRD and Raman analyses. Some spots rich in magnesium are also detected in both zones, the iron-rich one and the calcium-rich one. Some crystals rich

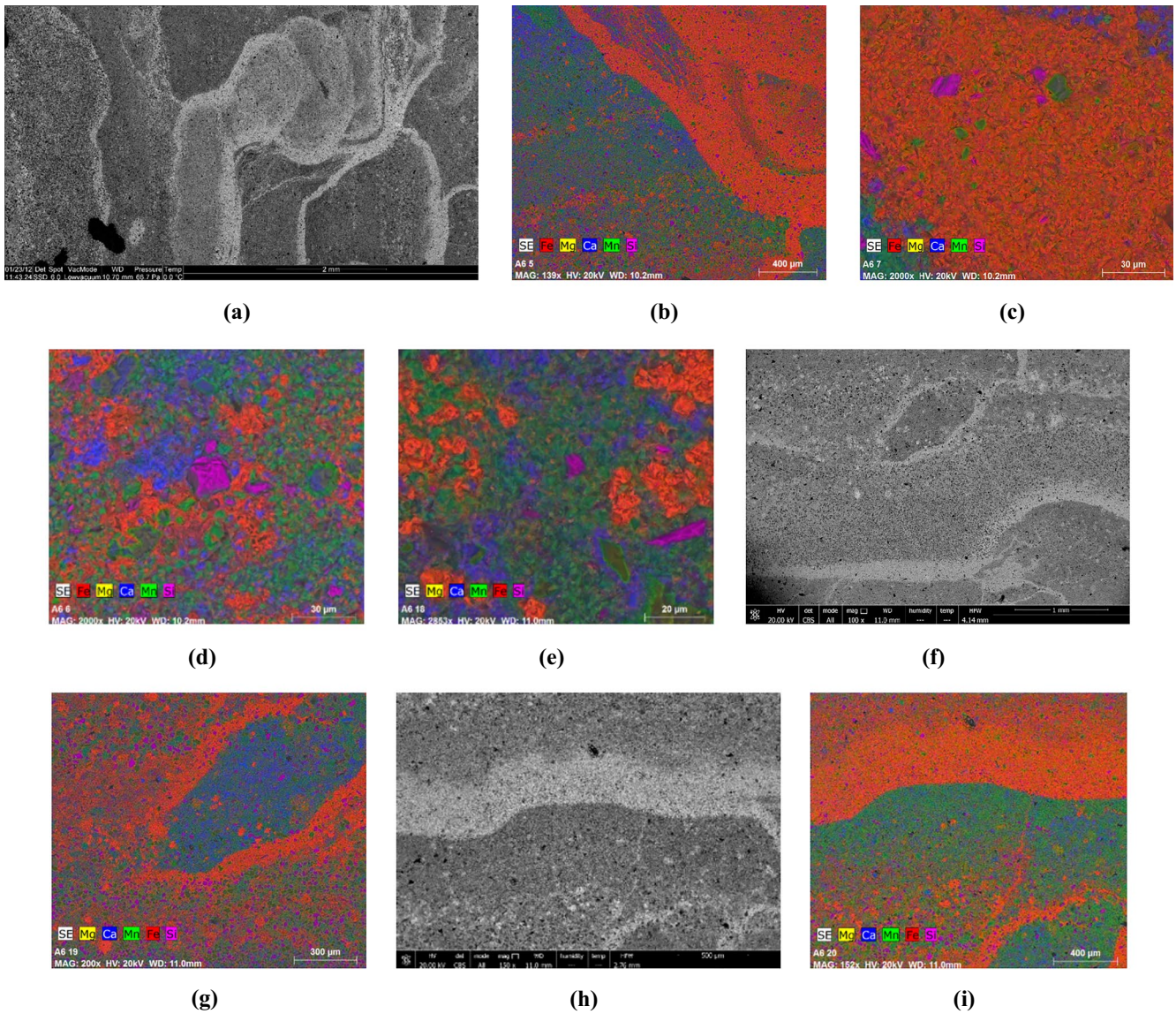

Figure 8. Electron micrographs of three regions of a thin polished layer from a section of the cylindrical tube. (a) BSE (Back-Scattered-Electron) image showing compositional changes over a large area. The brightest regions are richest in iron; (b) EDX map of the composition of the main elements found in the former zone; (c) the same augmented of a zone rich in Fe; (d) the same of a zone rich in Ca; (e) the same of a zone rich in Mn; (f) BSE image of another zone; (g) EDX map of the composition of the main elements found in the former zone; (h) BSE image of another zone; and (i) EDX map of the composition of the main elements found in the former zone (see Figures S2 and S3 of Supporting Information S1 for further partial compositional mappings).

in silicon are observed without other cations, which we can assign to quartz grains coming from sandy sediments trapped in the walls of these tubes (Figure 8b). In some zones calcium and magnesium are mixed due probably to the presence of dolomite crystals. In other zones a mixture of iron and magnesium is appreciated (orange zones) probably due to the formation of carbonates of iron and magnesium (Figure 8c). Some grains rich in calcium and surrounded by manganese are detected, probably from fossil remains surrounded by manganese oxides (Figure 8h). In general, calcium and iron are not mixed, hence the presence of ankerite is not probable. In many spots manganese is found along with magnesium, indicating the possible existence of kutnohorite rich in magnesium. Additional EDX mappings of partial elements of this sample are in Supporting Information S1 (Figure S2 in Supporting Information S1). These results are confirmed by semi-quantitative chemical analysis (Figure S3 in Supporting Information S1). In the gray zones of the section of the helicoidal tube (Figure 9), some fossils are detected formed by calcite, surrounded by iron and

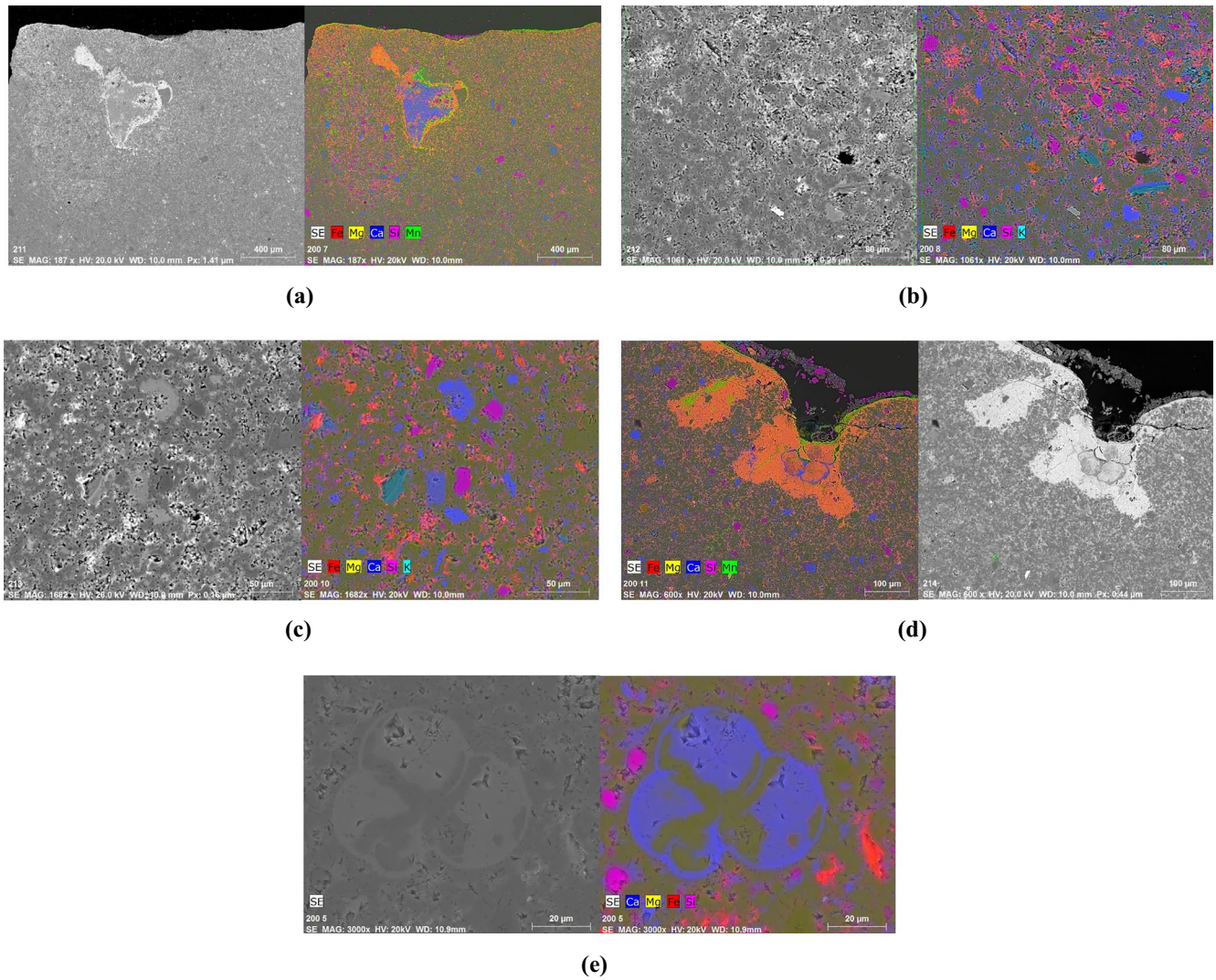

Figure 9. Back-Scattered-Electron micrographs of five zones of a section of the helicoidal sample together with compositional maps of the main elements found (see Figures S4 and S5 of Supporting Information S1 for further partial compositional mappings).

some spots of manganese. The background is mainly calcium/magnesium, probably dolomite or magnesian calcite with some spots of calcium belonging to calcite grains. In the external zones, edges and cracks, the presence of iron can correspond to the small proportion of pyrites observed in XRD. Some quartz grains are also detected with a few grains of silicon/aluminum, probably feldspars or micas. Additional EDX mappings of partial element compositions of a section of the helicoidal tube are shown in Figure S4 of Supporting Information S1. These results are confirmed by chemical analysis of some spots of the sample (Figure S5 in Supporting Information S1).

At present, we cannot predict precisely how fluid flow affects the mineralogy, crystal structure, and polymorph selection of precipitates. This is an active area of research (Balog et al., 2020; Nakouzi & Steinbock, 2016; Rauscher et al., 2018; Ziemecka et al., 2019) and we hope that future work will provide an enhanced understanding of how much the fluid flow has influenced the formation of the minerals found here. One notable aspect of one sample shown in Figure 5 is the helicoidal structure seen in the wall. A vortex in the flow in a tube can be induced by a twist in a given configuration. In this case, we have fluid flow accompanied by a precipitation reaction. Recent work with a laboratory chemical-garden-type setup has shown that a precipitation reaction in a thin tube can produce structures including helices in the precipitate (Knoll et al., 2019). While those experiments were in capillary tubes of much smaller diameter than the field

samples, and so the fluid Reynolds number in the two cases may be quite different, those laboratory results suggest a possible route to producing such helicoidal precipitate structures.

8. Conclusions

There is a large amount of literature discussing geological observations of horizontal fluid "plumbing" systems associated with methane seeps. Those papers are often discussing flow along these horizontal conduits. The common aspects of the geological papers that discuss horizontal undersea "plumbing" systems is that there is fluid arriving vertically toward the sea floor from below. Instead of exiting into the sea, it becomes blocked by some solid structure, which may be methane hydrates, clays, authigenic carbonates, vegetation mats, etc. Thus the fluid has to go somewhere, and is forced to travel horizontally. This is the basis of the analogy with a laboratory setup. In the geological instance we have flow from injection into a horizontal layer of porous medium; instead, in the laboratory, a Hele-Shaw cell.

An interesting aspect of the dynamics of this system is that the flow focuses into tubes that flow horizontally away from the injection point. Moreover, samples, like the ones we have analyzed here, show that carbonate rock tends to form around these tubes. This precipitation decreases any leakage from the walls of the tubes and continues to focus flow in tubes or filaments, as in the laboratory experiments. Is such a membrane necessarily always formed? Perhaps only in some instances; one might have a whole range of situations from viscous fingering in a porous medium, without a membrane, up to the situation with membrane being looked at here.

The laboratory two-dimensional chemical-garden experimental setup is a suitable starting point to discuss and interpret fluid-mechanical aspects of some interesting geological observations. Here, we have contributed to the question of seabed flow by setting out the evolution of these structures in fluid mechanical terms. From a fluid source under the sea, fluid starts flowing through a porous medium—a seep—it begins to wash the medium out and so to concentrate the flow in tubes—a mud volcano—on which the flow stops and block the conduit, and then restarts to find its exit blocked, forcing the spreading in a spider structure of horizontal tubes.

Authigenic biomineral carbonate formation is a significant component of the global carbon cycle (Alperin & Hoehler, 2010; Sun & Turchyn, 2014). There has been significant work carried out to understand the rates of the natural process (Ussler & Paull, 2008) and how it may be controlled by variables such as fluid flow rates (Karaca et al., 2010). Our work has relevance for understanding the mechanisms of the AOM in conditions of fluid flow (Alperin & Hoehler, 2010). From our work, considering the data on rates of AOM, and assuming a first-order reaction, the timescale for methane consumption is in the range $10^7 - 10^{13}$ s in the spider legs. On the other hand, the timescale for flow along a spider leg, is $\sim 1.6 \times 10^7$ s. Thus the ratio of flow timescale to reaction timescale—a species of Damköhler number—is between $: 10^{-6}$ and one. When methane decomposition is slower than the flow, this is allowing the release and decomposition of methane over a large surface area on the ocean floor. In terms of the biomineralization, our tubular samples are formed by silicic elements are cemented by carbonates. It has been noted that microstructures with a particular silicon-aluminum composition in these authigenic carbonates may be fossilized AOM consortia (Chen et al., 2014). Our analysis raises the possibility of geoengineering authigenic carbonate formation to decrease methane escape from the seabed by locking it into carbonate rocks through the addition of methanotrophic bacteria. A procedure might be to block the exit of methane seeps in an artificial analog of the natural process described above, and to add to the blocked zone a charge of the bacteria found in the natural situations. It remains to be studied whether such a process might contribute to programs of carbon capture and storage.

Data Availability Statement

Data supporting this study can be found in Supporting Information and are available online in the CSIC repository at http://dx.doi.org/10.20350/digitalCSIC/13998.

Acknowledgments
L. A. M. Rocha gratefully acknowledges funding from the Fundação para a Ciência e Tecnologia (FCT), Portugal (grant SFRH/BD/130401/2017). C. Pimentel acknowledges funding from Juan de la Cierva-Formación (grant FJC2018-035820-I) from the Spanish Ministry of Science. J. H. E. Cartwright and C. Ignacio Sainz-Díaz acknowledge the financial support of the Spanish MINCINN projects FIS2016-77692-C2-2-P and PCIN-2017-098. I. Sánchez-Almazo thanks the crew of the Cornide de Saavedra vessel, as well as the members of the Tasyo project, funded by the Spanish Marine Science and Technology Program, for allowing her to participate in the 2000–2001 Anastasya cruises. The authors acknowledge the contribution of the COST Action chemobrionics, CA17120.

References

Alperin, M., & Hoehler, T. (2010). The ongoing mystery of sea-floor methane. *Science*, *329*(5989), 288–289. https://doi.org/10.1126/science.1189966

Anderson, G. K. (2004). Enthalpy of dissociation and hydration number of methane hydrate from the Clapeyron equation. *The Journal of Chemical Thermodynamics*, *36*(12), 1119–1127. https://doi.org/10.1016/j.jct.2004.07.005

Balog, E., Papp, P., Tóth, Á., Horváth, D., & Schuszter, G. (2020). The impact of reaction rate on the formation of flow-driven confined precipitate patterns. *Physical Chemistry Chemical Physics*, *22*(24), 13390–13397. https://doi.org/10.1039/d0cp01036g

Barge, L. M., Cardoso, S. S. S., Cartwright, J. H. E., Cooper, G. J. T., Cronin, L., De Wit, A., et al. (2015). From chemical gardens to chemobrionics. *Chemical Reviews*, *115*(16), 8652–8703. https://doi.org/10.1021/acs.chemrev.5b00014

Barker, B., & Iversen, N. (1985). Anaerobic methane oxidation rates at the sulfate-methane transition in marine sediments from Kattegat and Skagerrak (Denmark). *Limnology & Oceanography*, *30*(5), 944–955. https://doi.org/10.4319/lo.1985.30.5.0944

Barnes, P. M., Lamarche, G., Bialas, J., Henrys, S., Pecher, I., Netzeband, G. L., et al. (2010). Tectonic and geological framework for gas hydrates and cold seeps on the Hikurangi subduction margin, New Zealand. *Marine Geology*, *272*(1–4), 26–48. https://doi.org/10.1016/j.margeo.2009.03.012

Barry, M. A., Boudreau, B. P., & Johnson, B. D. (2012). Gas domes in soft cohesive sediments. *Geology*, *40*(4), 379–382. https://doi.org/10.1130/g32686.1

Baumberger, T., Embley, R. W., Merle, S. G., Lilley, M. D., Raineault, N. A., & Lupton, J. E. (2018). Mantle-derived helium and multiple methane sources in gas bubbles of cold seeps along the Cascadia Continental Margin. *Geochemistry, Geophysics, Geosystems*, *19*(11), 4476–4486. https://doi.org/10.1029/2018GC007859

Blouet, J.-P., Imbert, P., & Foubert, A. (2017). Mechanisms of biogenic gas migration revealed by seep carbonate paragenesis, Panoche Hills, California. *AAPG Bulletin*, *101*(8), 1309–1340. https://doi.org/10.1306/10171616021

Bohrmann, G., & Torres, M. E. (2006). Gas hydrates in marine sediments. In *Marine geochemistry* (pp. 481–512). Springer. https://doi.org/10.1007/3-540-32144-6_14

Borromeo, L., Zimmermann, U., Andò, S., Coletti, G., Bersani, D., Basso, D., et al. (2017). Raman spectroscopy as a tool for magnesium estimation in Mg-calcite. *Journal of Raman Spectroscopy*, *48*(7), 983–992. https://doi.org/10.1002/jrs.5156

Brau, F., Haudin, F., Thouvenel-Romans, S., De Wit, A., Steinbock, O., Cardoso, S. S., & Cartwright, J. H. (2018). Filament dynamics in confined chemical gardens and in filiform corrosion. *Physical Chemistry Chemical Physics*, *20*(2), 784–793. https://doi.org/10.1039/c7cp06003c

Brennen, C. E. (2005). *Fundamentals of multiphase flow*. Cambridge University Press. https://doi.org/10.1017/CBO9780511807169

Buffett, B., & Archer, D. (2004). Global inventory of methane clathrate: Sensitivity to changes in the deep ocean. *Earth and Planetary Science Letters*, *227*(3–4), 185–199. https://doi.org/10.1016/j.epsl.2004.09.005

Bünz, S., Polyanov, S., Vadakkepuliyambatta, S., Consolaro, C., & Mienert, J. (2012). Active gas venting through hydrate-bearing sediments on the Vestnesa Ridge, offshore W-Svalbard. *Marine Geology*, *332–334*, 189–197. https://doi.org/10.1016/j.margeo.2012.09.012

Cardoso, S. S. S., & Cartwright, J. H. E. (2014). *Dynamics of osmosis in a porous medium Royal Society Open Science*. 1:140352. http://doi.org/10.1098/rsos.140352

Cardoso, S. S. S., Cartwright, J. H., Čejková, J., Cronin, L., Wit, A. D., Giannerini, S., et al. (2020). Chemobrionics: From self-assembled material architectures to the origin of life. *Artificial Life*, *26*(3), 315–326. https://doi.org/10.1162/artl_a_00323

Cardoso, S. S. S., & Cartwright, J. H. E. (2016). Increased methane emissions from deep osmotic and buoyant convection beneath submarine seeps as climate warms. *Nature Communications*, *7*, 13266. https://doi.org/10.1038/ncomms13266

Cartwright, J., & Santamarina, C. (2015). Seismic characteristics of fluid escape pipes in sedimentary basins: Implications for pipe genesis. *Marine and Petroleum Geology*, *65*, 126–140. https://doi.org/10.1016/j.marpetgeo.2015.03.023

Casenave, V. (2017). *Architecture et dynamique des migrations d'hydrocarbures dans une couverture sédimentaire à hydrates de gaz: Implications sur le système pétrolier (bassin du Bas Congo)* (PhD thesis). Université de Montpellier.

Casenave, V., Gay, A., & Imbert, P. (2017). Spider structures: Records of fluid venting from methane hydrates on the Congo continental slope. *Bulletin de la Societe Geologique de France*, *188*(4), 27. https://doi.org/10.1051/bsgf/2017189

Ceramicola, S., Dupré, S., Somoza, L., & Woodside, J. (2018). Cold seep systems. In *Submarine geomorphology* (pp. 367–387). Springer. https://doi.org/10.1007/978-3-319-57852-1_19

Chen, Y., Li, Y.-L., Zhou, G.-T., Li, H., Lin, Y.-T., Xiao, X., & Wang, F.-P. (2014). Biomineralization mediated by anaerobic methane-consuming cell consortia. *Scientific Reports*, *4*, 5696. https://doi.org/10.1038/srep05696

Collier, R. W., & Lilley, M. D. (2005). Composition of shelf methane seeps on the Cascadia Continental Margin. *Geophysical Research Letters*, *32*(6), 1–4. https://doi.org/10.1029/2004GL022050

Cooper, C., Crews, J., Schumer, R., Breitmeyer, R., Voepel, H., & Decker, D. (2014). Experimental investigation of transient thermal convection in porous media. *Transport in Porous Media*, *104*(2), 335–347. https://doi.org/10.1007/s11242-014-0337-0

Davie, M. K., & Buffett, B. A. (2003). Sources of methane for marine gas hydrate: Inferences from a comparison of observations and numerical models. *Earth and Planetary Science Letters*, *206*(1–2), 51–63. https://doi.org/10.1016/S0012-821X(02)01064-6

Davie, M. K., Zatsepina, O. Y., & Buffett, B. A. (2004). Methane solubility in marine hydrate environments. *Marine Geology*, *203*(1–2), 177–184. https://doi.org/10.1016/S0025-3227(03)00331-1

Di, P., Feng, D., & Chen, D. (2019). The distribution of dissolved methane and its air-sea flux in the plume of a seep field, Lingtou Promontory, South China Sea. *Geofluids*, *2019*, 1–12. https://doi.org/10.1155/2019/3240697

Díaz-del Río, V., Somoza, L., Martínez-Frías, J., Hernández-Molina, F. J., Lunar, R., Fernández-Puga, M. C., et al. (2001). Carbonate chimneys in the Gulf of Cadiz: Initial report of their petrography and geochemistry. In *Final proc. int. conf. geological processes on deep-water European margins, Moscow, Russia* (Vol. 175, pp. 53–54). UNESCO IOC Workshop Report.

Díaz-del Río, V., Somoza, L., Martínez-Frias, J., Mata, M. P., Delgado, A., Hernandez-Molina, F. J., et al. (2003). Vast fields of hydrocarbon-derived carbonate chimneys related to the accretionary wedge/olistostrome of the Gulf of Cádiz. *Marine Geology*, *195*, 177–200. https://doi.org/10.1016/s0025-3227(02)00687-4

Ding, Y., Gutiérrez-Ariza, C. M., Ignacio Sainz-Díaz, C., Cartwright, J. H., & Cardoso, S. S. (2019). Exploding chemical gardens: A phase-change clock reaction. *Angewandte Chemie - International Edition*, *58*(19), 6207–6213. https://doi.org/10.1002/anie.201812331

Englezos, P., Kalogerakis, N., Dholabhai, P. D., & Bishnoi, P. R. (1987). Kinetics of formation of methane and ethane gas hydrates. *Chemical Engineering Science*, *42*. https://doi.org/10.1016/0009-2509(87)87015-x

Feng, D., & Chen, D. (2015). Authigenic carbonates from an active cold seep of the northern South China Sea: New insights into fluid sources and past seepage activity. *Deep Sea Research Part II: Topical Studies in Oceanography*, *122*, 74–83. https://doi.org/10.1016/j.dsr2.2015.02.003

Floodgate, G. D., & Judd, A. G. (1992). The origins of shallow gas. *Continental Shelf Research*, *12*(10), 1145–1156. https://doi.org/10.1016/0278-4343(92)90075-U

Foschi, M., Cartwright, J. A., MacMinn, C. W., & Etiope, G. (2020). Evidence for massive emission of methane from a deep-water gas field during the Pliocene. *Proceedings of the National Academy of Sciences of the United States of America*, *117*(45), 27869–27876. https://doi.org/10.1073/pnas.2001904117

Fu, X., Jimenez-Martinez, J., Nguyen, T. P., William Carey, J., Viswanathan, H., Cueto-Felgueroso, L., & Juanes, R. (2020). Crustal fingering facilitates free-gas methane migration through the hydrate stability zone. *Proceedings of the National Academy of Sciences of the United States of America*, *117*(50), 31660–31664. https://doi.org/10.1073/pnas.2011064117

Gabitto, J. F., & Tsouris, C. (2010). Physical properties of gas hydrates: A review. *Journal of Thermodynamics*, *2010*(i), 1–12. https://doi.org/10.1155/2010/271291

Gay, A., Lopez, M., Potdevin, J.-L., Vidal, V., Varas, G., Favier, A., & Tribovillard, N. (2019). 3D morphology and timing of the giant fossil pockmark of Beauvoisin, se basin of France. *Journal of the Geological Society*, *176*(1), 61–77. https://doi.org/10.1144/jgs2018-064

Gay, A., & Migeon, S. (2017). Geological fluid flow in sedimentary basins. *Bulletin de la Societe Geologique de France*, *188*(4). https://doi.org/10.1051/bsgf/2017200

Giavarini, C., Maccioni, F., & Santarelli, M. L. (2003). Formation kinetics of propane hydrates. *Industrial & Engineering Chemistry Research*, *42*(7), 1517–1521. https://doi.org/10.1021/ie0207764

Gumerov, N., & Chahine, G. (1998). Dynamics of bubbles in conditions of gas hydrate formation. *Proceedings of the Eighth International Offshore and Polar Engineering Conference, Montreal, Canada*, 66–72.

Hammer, Ø., Nakrem, H. A., Little, C. T., Hryniewicz, K., Sandy, M. R., Hurum, J. H., et al. (2011). Hydrocarbon seeps from close to the Jurassic-Cretaceous boundary, Svalbard. *Palaeogeography, Palaeoclimatology, Palaeoecology*, *306*(1–2), 15–26. https://doi.org/10.1016/j.palaeo.2011.03.019

Herman, R. G., Bogdan, C. E., Sommer, A. J., & Simpson, D. R. (1987). Discrimination among carbonate minerals by Raman spectroscopy using the laser microprobe. *Applied Spectroscopy*, *41*(3), 437–440. https://doi.org/10.1366/0003702874448841

Herri, J. M., Pic, J. S., Gruy, F., & Cournil, M. (1999). Methane hydrate crystallization mechanism from in-situ particle sizing. *AIChE Journal*, *45*(3), 590–602. https://doi.org/10.1002/aic.690450316

Ho, S., Cartwright, J., & Imbert, P. (2012). Vertical evolution of fluid venting structures in relation to gas flux, in the Neogene-Quaternary of the Lower Congo Basin, Offshore Angola. *Marine Geology*, *332*, 40–55. https://doi.org/10.1016/j.margeo.2012.08.011

Hovland, M. (2002). On the self-sealing nature of marine seeps. *Continental Shelf Research*, *22*(16), 2387–2394. https://doi.org/10.1016/s0278-4343(02)00063-8

Joseph, A. (2016). *Investigating seafloors and oceans: From mud volcanoes to giant squid*. Elsevier.

Judd, A. G. (2003). The global importance and context of methane escape from the seabed. *Geo-Marine Letters*, *23*(3–4), 147–154. https://doi.org/10.1007/s00367-003-0136-z

Karaca, D., Hensen, C., & Wallmann, K. (2010). Controls on authigenic carbonate precipitation at cold seeps along the convergent margin off Costa Rica. *Geochemistry, Geophysics, Geosystems*, *11*(8). https://doi.org/10.1029/2010gc003062

Kedem, O., & Katchalsky, A. (1958). Thermodynamic analysis of the permeability of biological membranes to non-electrolytes. *Biochimica et Biophysica Acta*, *27*, 229–246. https://doi.org/10.1016/0006-3002(58)90330-5

Knoll, P., Gonzalez, A. V., McQueen, Z. C., & Steinbock, O. (2019). Flow-induced precipitation in thin capillaries creates helices, lamellae, and tubes. *Chemistry–A European Journal*, *25*(61), 13885–13889. https://doi.org/10.1002/chem.201903951

Koch, S., Berndt, C., Bialas, J., Haeckel, M., Crutchley, G., Papenberg, C., et al. (2015). Gas-controlled seafloor doming. *Geology*, *43*(7), 571–574. https://doi.org/10.1130/g36596.1

Kretschmer, K., Biastoch, A., Rüpke, L., & Burwicz, E. (2015). Modeling the fate of methane hydrates under global warming. *Global Biogeochemical Cycles*, *29*(5), 610–625. https://doi.org/10.1002/2014GB005011

Le Borgne, T., Dentz, M., & Villermaux, E. (2013). Stretching, coalescence, and mixing in porous media. *Physical Review Letters*, *110*(20), 204501. https://doi.org/10.1103/physrevlett.110.204501

Lee, J. D., Susilo, R., & Englezos, P. (2005). Methane-ethane and methane-propane hydrate formation and decomposition on water droplets. *Chemical Engineering Science*, *60*(15), 4203–4212. https://doi.org/10.1016/j.ces.2005.03.003

Liang, H., Chen, X., Wang, C., Zhao, D., & Weissert, H. (2016). Methane-derived authigenic carbonates of mid-cretaceous age in southern Tibet: Types of carbonate concretions, carbon sources, and formation processes. *Journal of Asian Earth Sciences*, *115*, 153–169. https://doi.org/10.1016/j.jseaes.2015.09.029

Liang, H., Song, Y., Chen, Y., & Liu, Y. (2011). The measurement of permeability of porous media with methane hydrate. *Petroleum Science and Technology*, *29*(1), 79–87. https://doi.org/10.1080/10916460903096871

Linga, P., Kumar, R., & Englezos, P. (2007). Gas hydrate formation from hydrogen/carbon dioxide and nitrogen/carbon dioxide gas mixtures. *Chemical Engineering Science*, *62*(16), 4268–4276. https://doi.org/10.1016/j.ces.2007.04.033

Linke, P., Suess, E., Torres, M., Martens, V., Rugh, W. D., Ziebis, W., & Kulm, L. D. (1994). In situ measurement of fluid flow from cold seeps at active continental margins. *Deep-Sea Research Part I*, *41*(4), 721–739. https://doi.org/10.1016/0967-0637(94)90051-5

Loher, M., Pape, T., Marcon, Y., Römer, M., Wintersteller, P., Praeg, D., et al. (2018). Mud extrusion and ring-fault gas seepage–upward branching fluid discharge at a deep-sea mud volcano. *Scientific Reports*, *8*(1), 1–11. https://doi.org/10.1038/s41598-018-24689-1

Lu, W., Chou, I. M., & Burruss, R. C. (2008). Determination of methane concentrations in water in equilibrium with sI methane hydrate in the absence of a vapor phase by in situ Raman spectroscopy. *Geochimica et Cosmochimica Acta*, *72*(2), 412–422. https://doi.org/10.1016/j.gca.2007.11.006

Luff, R., Wallmann, K., & Aloisi, G. (2004). Numerical modeling of carbonate crust formation at cold vent sites: Significance for fluid and methane budgets and chemosynthetic biological communities. *Earth and Planetary Science Letters*, *221*(1–4), 337–353. https://doi.org/10.1016/s0012-821x(04)00107-4

Maestrelli, D., Iacopini, D., Jihad, A. A., Bond, C. E., & Bonini, M. (2017). Seismic and structural characterization of fluid escape pipes using 3D and partial stack seismic from the loyal field (Scotland, UK): A multiphase and repeated intrusive mechanism. *Marine and Petroleum Geology*, *88*, 489–510. https://doi.org/10.1016/j.marpetgeo.2017.08.016

Magalhães, V. H., Pinheiro, L. M., Ivanov, M. K., Kozlova, E., Blinova, V., Kolganova, J., et al. (2012). Formation processes of methane-derived authigenic carbonates from the Gulf of Cadiz. *Sedimentary Geology*, *243*, 155–168. https://doi.org/10.1016/j.sedgeo.2011.10.013

Maia, A. R., Cartwright, J., & Andersen, E. (2016). Shallow plumbing systems inferred from spatial analysis of pockmark arrays. *Marine and Petroleum Geology*, *77*, 865–881. https://doi.org/10.1016/j.marpetgeo.2016.07.029

Mazzini, A., Ivanov, M. K., Nermoen, A., Bahr, A., Bohrmann, G., Svensen, H., & Planke, S. (2008). Complex plumbing systems in the near subsurface: Geometries of authigenic carbonates from Dolgovskoy Mound (Black Sea) constrained by analogue experiments. *Marine and Petroleum Geology*, *25*(6), 457–472. https://doi.org/10.1016/j.marpetgeo.2007.10.002

McMahon, S., van Smeerdijk Hood, A., & McIlroy, D. (2016). The origin and occurrence of subaqueous sedimentary cracks. *Geological Society, London, Special Publications*, *448*(1), 285–309. https://doi.org/10.1144/sp448.15

Meyer, D. W., Flemings, P. B., DiCarlo, D., You, K., Phillips, S. C., & Kneafsey, T. J. (2018). Experimental investigation of gas flow and hydrate formation within the hydrate stability zone. *Journal of Geophysical Research: Solid Earth*, *123*(7), 5350–5371. https://doi.org/10.1029/2018JB015748

Meyer, D. W., Flemings, P. B., You, K., & DiCarlo, D. A. (2020). Gas flow by invasion percolation through the hydrate stability zone. *Geophysical Research Letters*, *47*(3). https://doi.org/10.1029/2019gl084380

Milkov, A. V. (2004). Global estimates of hydrate-bound gas in marine sediments: How much is really out there? *Earth-Science Reviews*, *66*(3–4), 183–197. https://doi.org/10.1016/j.earscirev.2003.11.002

Monfort, J., & Nzihou, A. (1993). Light scattering kinetics study of cyclopropane hydrate growth. *Journal of Crystal Growth*, *128*, 1182–1186. https://doi.org/10.1016/s0022-0248(07)80120-5

Nakouzi, E., & Steinbock, O. (2016). Self-organization in precipitation reactions far from the equilibrium. *Science Advances*, *2*(8), e1601144. https://doi.org/10.1126/sciadv.1601144

Natarajan, V., Kalogerakis, N., & Engineering, P. (1994). Induction phenomena in gas hydrate. *Chemical Engineering Science*, *49*(13), 2075–2087. https://doi.org/10.1016/0009-2509(94)e0026-m

Nimblett, J., & Ruppel, C. (2003). Permeability evolution during the formation of gas hydrates in marine sediments. *Journal of Geophysical Research: Solid Earth*, *108*(B9). https://doi.org/10.1029/2001jb001650

O'Reilly, S. S., Hryniewicz, K., Little, C. T., Monteys, X., Szpak, M. T., Murphy, B. T., et al. (2014). Shallow water methane-derived authigenic carbonate mounds at the Codling Fault Zone, western Irish Sea. *Marine Geology*, *357*, 139–150. https://doi.org/10.1016/j.margeo.2014.08.007

Paganoni, M., Cartwright, J. A., Foschi, M., Shipp, C. R., & Van Rensbergen, P. (2018). Relationship between fluid-escape pipes and hydrate distribution in offshore Sabah (NW Borneo). *Marine Geology*, *395*, 82–103. https://doi.org/10.1016/j.margeo.2017.09.010

Parent, J. S., & Bishnoi, P. R. (1996). Investigations into the nucleation behaviour of methane gas hydrates. *Chemical Engineering Communications*, *144*(May), 51–64. https://doi.org/10.1080/00986449608936444

Peng, D. Y., & Robinson, D. B. (1976). A new two-constant equation of state. *Industrial and Engineering Chemistry Fundamentals*, *15*(1), 59–64. https://doi.org/10.1021/i160057a011

Petersen, C. J., Bünz, S., Hustoft, S., Mienert, J., & Klaeschen, D. (2010). High-resolution P-Cable 3D seismic imaging of gas chimney structures in gas hydrated sediments of an Arctic sediment drift. *Marine and Petroleum Geology*, *27*(9), 1981–1994. https://doi.org/10.1016/j.marpetgeo.2010.06.006

Phillips, O. M. (1991). *Flow and reactions in permeable rocks*. Cambridge University Press.

Prouty, N. G., Sahy, D., Ruppel, C. D., Roark, E. B., Condon, D., Brooke, S., et al. (2016). Insights into methane dynamics from analysis of authigenic carbonates and chemosynthetic mussels at newly-discovered Atlantic Margin seeps. *Earth and Planetary Science Letters*, *449*, 332–344. https://doi.org/10.1016/j.epsl.2016.05.023

Rashid, F., Glover, P. W., Lorinczi, P., Collier, R., & Lawrence, J. (2015). Porosity and permeability of tight carbonate reservoir rocks in the north of Iraq. *Journal of Petroleum Science and Engineering*, *133*, 147–161. https://doi.org/10.1016/j.petrol.2015.05.009

Räss, L., Simon, N. S., & Podladchikov, Y. Y. (2018). Spontaneous formation of fluid escape pipes from subsurface reservoirs. *Scientific Reports*, *8*(1), 1–11. https://doi.org/10.1038/s41598-018-29485-5

Rauscher, E., Schuszter, G., Bohner, B., Tóth, Á., & Horváth, D. (2018). Osmotic contribution to the flow-driven tube formation of copper-phosphate and copper-silicate chemical gardens. *Physical Chemistry Chemical Physics*, *20*(8), 5766–5770. https://doi.org/10.1039/c7cp08282g

Reeburgh, W. S. (1980). Anaerobic methane oxidation: Rate depth distributions in Skan Bay sediments. *Earth and Planetary Science Letters*, *47*(3), 345–352. https://doi.org/10.1016/0012-821X(80)90021-7

Reeburgh, W. S. (2007). Oceanic methane biogeochemistry. *Chemical Reviews*, *107*, 486–513. https://doi.org/10.1021/cr050362v

Rehder, G., Brewer, P. W., Peltzer, E. T., & Friederich, G. (2002). Enhanced lifetime of methane bubble streams within the deep ocean. *Geophysical Research Letters*, *29*(15), 21-1–21-4. https://doi.org/10.1029/2001gl013966

Reynolds, P., Planke, S., Millett, J., Jerram, D. A., Trulsvik, M., Schofield, N., & Myklebust, R. (2017). Hydrothermal vent complexes offshore northeast Greenland: A potential role in driving the PETM. *Earth and Planetary Science Letters*, *467*, 72–78. https://doi.org/10.1016/j.epsl.2017.03.031

Ribeiro, C. P., & Lage, P. L. (2008). Modelling of hydrate formation kinetics: State-of-the-art and future directions. *Chemical Engineering Science*, *63*(8), 2007–2034. https://doi.org/10.1016/j.ces.2008.01.014

Riedel, M., Crutchley, G., Koch, S., Berndt, C., Bialas, J., Eisenberg-Klein, G., et al. (2018). Elongate fluid flow structures: Stress control on gas migration at Opouawe Bank, New Zealand. *Marine and Petroleum Geology*, *92*, 913–931. https://doi.org/10.1016/j.marpetgeo.2018.03.029

Riedel, M., Scherwath, M., Römer, M., Veloso, M., Heesemann, M., & Spence, G. D. (2018). Distributed natural gas venting offshore along the Cascadia margin. *Nature Communications*, *9*(1). https://doi.org/10.1038/s41467-018-05736-x

Rocha, L. A. M., Cartwright, J. H. E., & Cardoso, S. S. S. (2021). Filament dynamics in planar chemical gardens. *Physical Chemistry Chemical Physics*, *23*, 5222–5235. https://doi.org/10.1039/D0CP03674A

Ruppel, C. D., & Kessler, J. D. (2017). The interaction of climate change and methane hydrates. *Reviews of Geophysics*, *55*(1), 126–168. https://doi.org/10.1002/2016RG000534

Serov, P., Vadakkepuliyambatta, S., Mienert, J., Patton, H., Portnov, A., Silyakova, A., et al. (2017). Postglacial response of Arctic Ocean gas hydrates to climatic amelioration. *Proceedings of the National Academy of Sciences*, *114*(24), 6215–6220. https://doi.org/10.1073/pnas.1619288114

Shah, S., Yang, J., Crawshaw, J., Gharbi, O., & Boek, E. (2013). Predicting porosity and permeability of carbonate rocks from pore- to core-scale using medical CT, confocal laser scanning microscopy and micro CT. *Proceedings - SPE Annual Technical Conference and Exhibition*, *3*. https://doi.org/10.2118/166252-MS

Shakhova, N., Semiktov, I., Salyuk, A., Yusupov, V., Kosmach, D., & Gustafsson, Ö. (2010). Extensive methane venting to the atmosphere from sediments of the East Siberian Arctic shelf. *Science*, *327*, 1246–1250. https://doi.org/10.1126/science.1182221

Shimizu, H., Kumazaki, T., Kume, T., & Sasaki, S. (2002). Elasticity of single-crystal methane hydrate at high pressure. *Physical Review B*, *65*(21), 9–12. https://doi.org/10.1103/physrevb.65.212102
Silva-Bedoya, L. M., Watkin, E., & Machuca, L. L. (2021). Deep-sea corrosion rusticles from iron-hulled shipwrecks. *Materials and Corrosion*, *72*(7), 1138–1151. https://doi.org/10.1002/maco.202112289
Skarke, A., Ruppel, C., Kodis, M., Brothers, D., & Lobecker, E. (2014). Widespread methane leakage from the sea floor on the northern US Atlantic margin. *Nature Geoscience*, *7*(9), 657–661. https://doi.org/10.1038/ngeo2232
Skovborg, P., & Rasmussen, P. (1994). A mass transport limited model for the growth of methane and ethane gas hydrates. *Chemical Engineering Science*, *49*(8), 1131–1143. https://doi.org/10.1016/0009-2509(94)85085-2
Sloan, E. D., & Koh, C. (2007). *Clathrate hydrates of natural gases* (3rd ed., Vol. 20074156). Marcel Dekker. Retrieved from https://www.taylorfrancis.com/books/9781420008494
Solomon, E. A., Kastner, M., MacDonald, I. R., & Leifer, I. (2009). Considerable methane fluxes to the atmosphere from hydrocarbon seeps in the Gulf of Mexico. *Nature Geoscience*, *2*(8), 561–565. https://doi.org/10.1038/ngeo574
Sultan, N., Foucher, J. P., Cochonat, P., Tonnerre, T., Bourillet, J. F., Ondreas, H., et al. (2004). Dynamics of gas hydrate: Case of the Congo continental slope. *Marine Geology*, *206*(1–4), 1–18. https://doi.org/10.1016/j.margeo.2004.03.005
Sun, X., & Turchyn, A. V. (2014). Significant contribution of authigenic carbonate to marine carbon burial. *Nature Geoscience*, *7*(3), 201–204. https://doi.org/10.1038/ngeo2070
Sun, Y., Peckmann, J., Hu, Y., Wang, X., Gong, S., Peng, Y., et al. (2020). Formation of tubular carbonates within the seabed of the northern South China Sea. *Minerals*, *10*(9), 768. https://doi.org/10.3390/min10090768
Talimi, V., Muzychka, Y., & Kocabiyik, S. (2012). A review on numerical studies of slug flow hydrodynamics and heat transfer in microtubes and microchannels. *International Journal of Multiphase Flow*, *39*, 88–104. doi:https://doi.org/10.1016/j.ijmultiphaseflow.2011.10.005
Timoshenko, S., & Woinowsky-Krieger, S. (1959). *Theory of plates and shells*: McGraw-Hill.
Tishchenko, P., Hensen, C., Wallmann, K., & Wong, C. S. (2005). Calculation of the stability and solubility of methane hydrate in seawater. *Chemical Geology*, *219*(1–4), 37–52. https://doi.org/10.1016/j.chemgeo.2005.02.008
Todd, A. C., & MacDonald, I. R. (2017). Time series video analysis of bubble release processes at natural hydrocarbon seeps in the Northern Gulf of Mexico. *Marine and Petroleum Geology*, *82*, 21–34. https://doi.org/10.1016/j.marpetgeo.2017.01.014
Treude, T., Boetius, A., Knittel, K., Wallmann, K., & Jørgensen, B. B. (2003). Anaerobic oxidation of methane above gas hydrates at Hydrate Ridge, NE Pacific Ocean. *Marine Ecology Progress Series*, *264*, 1–14. https://doi.org/10.3354/meps264001
Treude, T., Orphan, V., Knittel, K., Gieseke, A., House, C. H., & Boetius, A. (2007). Consumption of methane and CO_2 by methanotrophic microbial mats from gas seeps of the anoxic Black Sea. *Applied and Environmental Microbiology*, *73*(7), 2271–2283. https://doi.org/10.1128/AEM.02685-06
Turcotte, D. L., & Schubert, G. (2002). *Geodynamics* (2nd ed.). Cambridge University Press.
Ussler, W., & Paull, C. K. (2008). Rates of anaerobic oxidation of methane and authigenic carbonate mineralization in methane-rich deep-sea sediments inferred from models and geochemical profiles. *Earth and Planetary Science Letters*, *266*(3–4), 271–287. https://doi.org/10.1016/j.epsl.2007.10.056
Vysniauskas, A., & Bishnoi, P. R. (1983). A kinetic study of methane hydrate formation. *Chemical Engineering Science*, *38*(7), 1061–1072. https://doi.org/10.1016/0009-2509(83)80027-X
Wagatsuma, S., Higashi, T., Sumino, Y., & Achiwa, A. (2017). Pattern of a confined chemical garden controlled by injection speed. *Physical Review E*, *95*(5). https://doi.org/10.1103/PhysRevE.95.052220
Weaire, D., & Hutzler, S. (2001). *The physics of foams*. Clarendon Press. Retrieved from https://books.google.pt/books?id=mEHlZ9ZodFsC
Wei, Z., Xu, T., Shang, S., Tian, H., Cao, Y., Wang, J., et al. (2021). Laboratory experimental study on the formation of authigenic carbonates induced by microbes in marine sediments. *Journal of Marine Science and Engineering*, *9*(5). https://doi.org/10.3390/jmse9050479
Wood, W. T., Gettrust, J. F., Chapman, N. R., Spence, G. D., & Hyndman, R. D. (2002). Decreased stability of methane hydrates in marine sediments owing to phase-boundary roughness. *Nature*, *420*(6916), 656–660. https://doi.org/10.1038/nature01263
Xu, T., Bei, K., Tian, H., & Cao, Y. (2017). Laboratory experiment and numerical simulation on authigenic mineral formation induced by seabed methane seeps. *Marine and Petroleum Geology*, *88*, 950–960. https://doi.org/10.1016/j.marpetgeo.2017.09.025
Ye, Y., Chiogna, G., Cirpka, O. A., Grathwohl, P., & Rolle, M. (2015). Enhancement of plume dilution in two-dimensional and three-dimensional porous media by flow focusing in high-permeability inclusions. *Water Resources Research*, *51*(7), 5582–5602. https://doi.org/10.1002/2015WR016962
Zhang, X.-H., Lu, X.-B., Zhang, L.-M., Wang, S.-Y., & Li, Q.-P. (2012). Experimental study on mechanical properties of methane-hydrate-bearing sediments. *Acta Mechanica Sinica*, *28*(5), 1356–1366. https://doi.org/10.1007/s10409-012-0142-3
Ziemecka, I., Brau, F., & De Wit, A. (2020). Confined direct and reverse chemical gardens: Influence of local flow velocity on precipitation patterns. *Chaos*, *30*(1), 013140. https://doi.org/10.1063/1.5128107
Ziemecka, I., Gokalp, S., Stroobants, S., Brau, F., Maes, D., & De Wit, A. (2019). Polymorph selection of Roy by flow-driven crystallization. *Crystals*, *9*(7). https://doi.org/10.3390/cryst9070351